Available online at www.sciencedirect.com
ScienceDirect
Comput. Methods Appl. Mech. Engrg. 364 (2020) 112958
Computer methods in applied mechanics and engineering
www.elsevier.com/locate/cma

The Hot Optimal Transportation Meshfree (HOTM) method for materials under extreme dynamic thermomechanical conditions

Hao Wang[a], Huming Liao[b], Zongyue Fan[a], Jiang Fan[b], Laurent Stainier[c], Xiaobai Li[d], Bo Li[a,*]

[a] *Department of Mechanical and Aerospace Engineering, Case Western Reserve University, Cleveland, OH 44106, USA*
[b] *School of Energy and Power Engineering, Beihang University, Beijing 100191, China*
[c] *Research Institute in Civil and Mechanical Engineering (GeM, UMR 6183 CNRS), Ecole Centrale de Nantes, 1 rue de la Noë, Nantes, France*
[d] *Robert Bosch LLC, 384 Santa Trinita Ave, Sunnyvale, CA 94085, USA*

Received 9 April 2019; received in revised form 12 February 2020; accepted 20 February 2020
Available online xxxx

Abstract

We present a monolithic incremental Lagrangian framework based on meshfree methods, the Hot Optimal Transportation Meshfree (HOTM) method, for a robust and efficient solution of the dynamic response of materials under extreme thermomechanical conditions, possibly involving extremely large deformation, phase transition and multiphase mixing. The HOTM method combines the Optimal Transportation Meshfree (OTM) method and the variational thermomechanical constitutive updates. The variational structure of a dynamic system with general internal dissipative mechanisms is discretized in time by applying the Optimal Transportation theory, while material points and nodes are introduced for the spatial discretization. A phase-aware constitutive model is developed to describe the history-dependent material behavior in various phases due to melting, vaporization and solidification. The fully discretized conservation equations of linear momentum and energy are solved simultaneously using an operator splitting algorithm to predict the deformation, temperature and internal variables of the computational domain. The convergence property of the meshfree solution of the energy conservation equation is studied in a three-dimensional transient heat conduction problem by comparing to the analytical solutions. Accuracy of the HOTM method is also assessed in the example of upsetting a metallic billet up to a compression ratio of 95% under various external heating and cooling strategies. The scope and robustness of the HOTM method are demonstrated in the application of the laser cladding technology.

Keywords: Thermomechanical coupling; Meshfree methods; OTM method; Extremely large deformation; Phase transition; Additive manufacturing

1. Introduction

Extreme dynamic thermomechanical conditions are commonly experienced by materials in a wide range of industrial applications, such as manufacturing, new energy technologies, defense and national security. In particular, increasing interest in strongly coupled thermomechanical problems is driven by the recent rapid advances

* Corresponding author.
E-mail addresses: hxw357@case.edu (H. Wang), liaohuming@buaa.edu.cn (H. Liao), zxf57@case.edu (Z. Fan), fanjiang@buaa.edu.cn (J. Fan), Laurent.Stainier@ec-nantes.fr (L. Stainier), xiaobai.li2@us.bosch.com (X. Li), bxl295@case.edu (B. Li).

https://doi.org/10.1016/j.cma.2020.112958
0045-7825/

in materials fabrication by additive manufacturing(AM) processes. These processes usually involve extremely large deformations, large temperature gradient and high heating/cooling rates, highly nonlinear inelastic material responses, and phase transition, such as melting, vaporization and solidification. Thus, high fidelity predictions of the dynamic response of materials under extreme thermomechanical coupling conditions have arisen as one of the major challenges in computational mechanics.

There are various thermomechanical coupling models for the phase change problem in welding simulations [1,2]. Similar numerical approaches can also be found in the studies of residual stresses in the casting process [3,4]. Furthermore, numerical simulations play a significant role in the fundamental understanding of emerging additive manufacturing technologies. Detailed reviews can be found for instance in [5,6] and [7]. Nevertheless, grid-based Lagrangian approaches, for example, total or updated Lagrangian Finite Element method, suffer from challenges in dealing with large deformation unconstrained flows of the type encountered during manufacturing processes due to mesh entanglement. These difficulties are compounded in problems with phase transition and multiphase mixing arising from applications such as additive manufacturing, casting, high speed forming and high rate machining [8–13]. Traditional Eulerian framework, including Eulerian Finite Element method, Finite Difference and Finite Volume methods, for the description of unconstrained flows becomes awkward when the flow involves variable multiphase domains, free-surface boundary conditions, dynamic contact as well as history-dependent thermomechanical material behavior [14,15]. Another conventional approach uses the Arbitrary Lagrangian–Eulerian formulation (ALE) [15–17], which combines the advantages of both Lagrangian and Eulerian methods. However, the ALE method is limited for large localized deformation in unconstrained multiphase flows, and remeshing and remapping of state variables are still necessary for such scenarios.

Alternatively, meshfree methods with Lagrangian kernels furnish effective means of addressing the challenges of mesh tangling and distortion when dealing with large deformations, since they do not require a mesh. A variety of meshfree methods can be found in the literature, including Smoothed Particle Hydrodynamics (SPH) [18–20], Discrete Element Method (DEM) [21,22], Finite Pointset Method (FPM) [23,24], Element Free Galerkin Method (EFGM) [25,26], Reproducing Kernel Particle Method (RKPM) [27–30], Meshless Local Petrov–Galerkin Method (MLPG) [31,32], Particle Finite Element Method (PFEM) [33], Material Point Method (MPM) [34–36] and more (see the recent review in [37]). Among the meshfree methods, the Optimal Transportation Meshfree (OTM) method proposed by Li and Ortiz in [38] provides a robust and efficient solution to predict the thermomechanical response of materials under extreme dynamic conditions, especially in adiabatic circumstances [39–42]. Recently, researchers have studied the capability of the meshfree methods to model severe material flows combining with phase transition and multiphase mixing induced by high cooling and heating rates. For instance, a DEM framework is developed by Ganeriwala and Zohdi to simulate a single laser track of the selective laser melting (SLM) process [43]. SPH simulations of the SLM process of metallic particles were presented in [44] to investigate the influence of laser power on the melt pool dimensions and thermodynamics. Fürstenau et al. [45] developed an SPH framework based on the GPU implementation of DualSPHysics for SLM powder-scale simulations to quantify the melt pool characteristics as a function of processing parameters. Wessels et al. presented a computational framework to model the thermomechanical process with phase change in additive manufacturing technologies based on the OTM method and virtual work principle [46,47]. However, the mathematical formulation for strong non-equilibrium thermomechanical coupling problems involving inelasticity and general internal dissipation mechanisms, such as plasticity, has not been fully demonstrated in a meshfree framework.

The OTM method is constructed through an integration of optimal transportation theory [48] with Local Maximum Entropy (LME) meshfree interpolation [49] and material point sampling method [34]. The optimal transportation theory results in a geometrically exact time discretization of the action with conservative properties of the mass and linear momentum, thus bypassing the need for solving a costly Poisson equation for the pressure and eliminating the mass conservation errors that afflict Eulerian formulations. With the introduction of the LME shape function, a weak Kronecker-delta property is satisfied on the boundary, which enables the direct imposition of essential boundary conditions. In addition, the dynamic reconnection of material points and nodes requires no remapping of history variables but overcomes the challenges of mesh entanglement and distortion. Foca et al. studied the influence of the location as well as the ratio between the material points and nodes in the dynamic connection on the accuracy of the OTM method [50]. In case of an under integration scheme employed to distribute the material points and nodes, Weissenfels and Wriggers proposed a stabilized OTM method to alleviate the spurious mode in the computations [51]. The combination of these features ensures enhanced stability and robustness of the OTM method in the simulations of large deformations and fluid interacting with highly flexible structures [52].

On the other hand, a variational formulation for general coupled thermomechanical problems in dissipative materials under quasistatic loading conditions is presented by Yang et al. [53] and further developed by Stainier et al. [54–56]. The authors show that there exists a potential function such that both the conservation of energy and balance of linear momentum, boundary and initial conditions and even the evolutions of internal variables are obtained as the Euler–Lagrange equations of its first variation. This variational approach presents many attractive features, such as unicity, convergence and stability of the formulations for the strong coupling of thermomechanical boundary value problems, including finite elastoplastic deformation, non-Newtonian viscosity, rate sensitivity, arbitrary flow and hardening rule, as well as heat conduction. Although inertia effects are not the main focus of this variational principle, it gives encouraging results for general dissipative systems when coupled with LME shape functions [50].

In this paper, we aim to develop a monolithic Lagrangian meshfree computational scheme, the Hot Optimal Transportation Meshfree (HOTM) method, for a dynamic system under extreme thermomechanical conditions involving extremely large deformations and dynamic phase transition. Following the local thermodynamic model [56], we construct a phase-aware constitutive relation to describe the dynamic response of materials including finite deformation, viscoelastoplastic behavior with strain hardening, thermal softening and rate sensitivity, general equation of state and dissipation mechanisms covering the solid, liquid and gas phases. We then extend the variational formulation of the strongly coupled thermomechanical problem by including the inertia effects. The proposed variational structure of a dynamic dissipative system can be rewritten in an incremental form with the aid of the incremental effective energy density and the Optimal Transportation theory for the time discretization of the kinetic energy. The stationarity conditions of the variational principle yield the semi-discrete energy conservation and balance of linear momentum equations. By introducing the material point integration scheme and using the LME shape functions to interpolate the materials local state at the material points from the neighboring nodal degrees of freedom, we can derive the fully discrete mechanical and thermal balance equations in a meshfree solution. To this end, an operator splitting algorithm is employed to solve the fully discrete balance equations and compute the evolution of the deformation, temperature and internal variables simultaneously. In specific, the mechanical balance equations are solved explicitly, while the thermal equilibrium equations solved by an implicit method using Newton–Raphson iterations. By leveraging on the monolithic meshfree solution of the conservation equations and the powerful theories in the calculus of variations, the proposed HOTM method effectively addresses some of the drawbacks in the current state-of-the-art algorithms for strongly coupled thermomechanical problems, such as loose coupling, convergence issues, and instabilities.

Finally, we demonstrate the accuracy and convergence property of the HOTM method in the example of three-dimensional transient heat transfer problem with analytical solutions. Validation of the proposed computational framework is performed by directly comparing the predicted results by the HOTM method to the data presented by Simo et al. [8] in the application of upsetting a metallic billet under various thermomechanical boundary conditions. The robustness and versatility of the HOTM method are further illustrated in the study of the correlation between the processing parameters and cladding formation in the laser cladding technology. Application of the HOTM method in other additive manufacturing technologies can be found in [57] as well.

2. General framework

This section presents the construction of the Hot Optimal Transportation Meshfree (HOTM) method, including the variational formulation of a dynamic thermomechanical dissipative system and the meshfree discretization scheme. We extend the general modeling framework for thermomechanical coupling problems proposed by Stainier [56] to account for the phase transition, such as melting, vaporization, and solidification. The variational formulation with inertia effects is then developed and discretized within the Optimal Transportation Meshfree (OTM) framework. The fully discretized governing equations are solved by the explicit–implicit method to predict the evolution of the deformation, local state variables and temperature distribution in the computational domain.

2.1. Phase-aware constitutive models

Consider a general thermomechanical process undergone by a continuous body of reference configuration $\Omega_0 \subset \Re^3$. The motion of the body is described by the deformation mapping $\boldsymbol{\varphi} : \Omega_0 \times [t_0, t_f] \rightarrow \Re^3$, where $[t_0, t_f]$ is the time interval elapsed during the motion. Material points in the reference configuration are denoted by

$\boldsymbol{X} \in \Omega_0$ mapping to points $\boldsymbol{x} = \boldsymbol{\varphi}(\boldsymbol{X}, t)$ in the deformed configuration $\Omega_t = \boldsymbol{\varphi}(\Omega_0, t)$. The mechanical state of the material system is defined by the deformation gradient $\boldsymbol{F}$ as

$$\boldsymbol{F}(\boldsymbol{X}, t) = \nabla_0 \boldsymbol{\varphi}(\boldsymbol{X}, t) \quad \text{in } \Omega_0 \times [t_0, t], \tag{1}$$

where ∇_0 denotes the partial derivatives of the motion with respect to the reference configuration. In addition, the variables describing the thermal state are the temperature $T : \Omega_0 \times [t_0, t] \to \Re^+$ and a vector $\boldsymbol{G}$ taking the form:

$$\boldsymbol{G} = -\frac{1}{T} \nabla_0 T. \tag{2}$$

A local-state approach is introduced to describe the thermomechanical process with general dissipation mechanisms. In specific, we postulate the existence of a Helmholtz free energy density (per unit undeformed volume) $A(\boldsymbol{F}, T, \boldsymbol{Z})$ given by

$$A(\boldsymbol{F}, T, \boldsymbol{Z}) = \inf_N \{U(\boldsymbol{F}, N, \boldsymbol{Z}) - TN\}, \tag{3}$$

where $\boldsymbol{Z}$ is a set of internal variables for the local state of the material, and U and N are the internal energy density and the entropy density, respectively. We shall denote the first Piola–Kirchhoff stress tensor by $\boldsymbol{P}$ and the forces conjugated to internal variables by $\boldsymbol{Y}$. The total stress tensor and the driving forces of the internal variables are assumed to follow the additive decomposition as

$$\boldsymbol{P} = \boldsymbol{P}^e + \boldsymbol{P}^v, \tag{4}$$

$$\boldsymbol{Y} = \boldsymbol{Y}^e + \boldsymbol{Y}^d, \tag{5}$$

where $\boldsymbol{P}^e$ and $\boldsymbol{P}^v$ are the equilibrium and viscous part of the stress, and $\boldsymbol{Y}^e$ and $\boldsymbol{Y}^d$ are the equilibrium and dissipative part of the driving forces, respectively. By Coleman's relations, we obtain

$$N = -\frac{\partial A}{\partial T}(\boldsymbol{F}, T, \boldsymbol{Z}), \tag{6}$$

$$\boldsymbol{P}^e = \frac{\partial A}{\partial \boldsymbol{F}}(\boldsymbol{F}, T, \boldsymbol{Z}), \tag{7}$$

$$\boldsymbol{Y}^e = \frac{\partial A}{\partial \boldsymbol{Z}}(\boldsymbol{F}, T, \boldsymbol{Z}). \tag{8}$$

In order to determine the evolution of the internal variables, we further assume the existence of a viscous dissipation pseudo-potential $\phi^*(\dot{\boldsymbol{F}}; \boldsymbol{F}, T, \boldsymbol{Z})$, a kinetic dissipation pseudo-potential $\psi^*(\dot{\boldsymbol{Z}}; \boldsymbol{F}, T, \boldsymbol{Z})$ and a heat dissipation potential $\chi(\boldsymbol{G}; \boldsymbol{F}, T, \boldsymbol{Z})$ [58,59], which leads to the definition of the viscous stress tensor, the dissipative part of the driving force of the internal variables and the heat conduction induced heat flux, $\boldsymbol{q}$, as

$$\boldsymbol{P}^v = \frac{\partial \phi^*}{\partial \dot{\boldsymbol{F}}}(\dot{\boldsymbol{F}}; \boldsymbol{F}, T, \boldsymbol{Z}). \tag{9}$$

$$\boldsymbol{Y}^d = \frac{\partial \psi^*}{\partial \dot{\boldsymbol{Z}}}(\dot{\boldsymbol{Z}}; \boldsymbol{F}, T, \boldsymbol{Z}), \tag{10}$$

and

$$\boldsymbol{q} = \frac{\partial \chi}{\partial \boldsymbol{G}}(\boldsymbol{G}; \boldsymbol{F}, T, \boldsymbol{Z}), \tag{11}$$

respectively. Note that the internal variables should not produce any work. Thus we have

$$\boldsymbol{Y} \cdot \dot{\boldsymbol{Z}} = (\boldsymbol{Y}^e + \boldsymbol{Y}^d) \cdot \dot{\boldsymbol{Z}} = 0 \quad \text{for } \forall \dot{\boldsymbol{Z}}, \tag{12}$$

which yields

$$\boldsymbol{Y}^e = -\boldsymbol{Y}^d \tag{13}$$

Finally, the local total dissipation pseudo-potential denoted by Δ, can be decomposed additively into three parts as

$$\Delta(\dot{\boldsymbol{F}}, \dot{\boldsymbol{Z}}, \boldsymbol{G}; \boldsymbol{F}, \boldsymbol{Z}, T) = \phi^* + \psi^* - \chi. \tag{14}$$

As a result, the total stresses and driving forces for the internal variables follow in the form

$$\boldsymbol{P} = \frac{\partial A}{\partial \boldsymbol{F}}(\boldsymbol{F}, T, \boldsymbol{Z}) + \frac{\partial \Delta}{\partial \dot{\boldsymbol{F}}}(\dot{\boldsymbol{F}}, \dot{\boldsymbol{Z}}, \boldsymbol{G}), \tag{15}$$

$$\boldsymbol{Y} = -\frac{\partial A}{\partial \boldsymbol{Z}}(\boldsymbol{F}, T, \boldsymbol{Z}) + \frac{\partial \Delta}{\partial \dot{\boldsymbol{Z}}}(\dot{\boldsymbol{F}}, \dot{\boldsymbol{Z}}, \boldsymbol{G}) = 0, \tag{16}$$

Given the Helmholtz free energy density and the total dissipation pseudopotential, the constitutive models presented above in Eqs. (15) and (16) are general enough to describe materials dynamic behavior under arbitrary thermomechanical boundary conditions. However, in response to the extreme dynamic thermomechanical coupling conditions, materials usually experience extremely large deformations and high temperature variations, which often results in highly nonlinear inelastic behavior and phase change, such as melting, vaporization, and solidification. Based on the local thermodynamic models, we construct a specific form for the constitutive relation of materials (e.g., metals) possibly involving finite-deformation, an arbitrary equation of state, thermo-elasticity and thermo-viscoplasticity, multiphase transition and mixing, and allowing to study the partition of plastic work in stored and dissipated energy in a systematic fashion. To this end, we follow the multiplicative elastic–plastic kinematics suggested by Lee [60] and further developed by many others to decompose the deformation gradient as

$$\boldsymbol{F} = \boldsymbol{F}^e \boldsymbol{F}^p, \tag{17}$$

where $\boldsymbol{F}^e$ and $\boldsymbol{F}^p$ are the elastic and plastic deformation, respectively. We then introduce a scalar internal variable, $\bar{\epsilon}^p$, to measure the cumulated plastic strain in a macroscopic plasticity model of the von Mises type. The plastic flow rule for von Mises plasticity can be stated as

$$\boldsymbol{L}^p = \dot{\boldsymbol{F}}^p \boldsymbol{F}^{p-1} = \dot{\bar{\epsilon}}^p \boldsymbol{M}, \tag{18}$$

where the direction tensor $\boldsymbol{M}$ is a symmetric tensor such that the normalization conditions and isochoricity of plastic flow are satisfied, i.e.,

$$\boldsymbol{M} \cdot \boldsymbol{M} = \frac{3}{2} \quad \text{and} \quad tr[\boldsymbol{M}] = 0. \tag{19}$$

In materials such as metals, the elastic response and the specific heat are ostensibly independent of the internal processes and the Helmholtz free energy density decomposes additively as

$$A = W^{e,vol}(J, T) + W^{e,dev}(\boldsymbol{F}\boldsymbol{F}^{p-1}, T) + W^p(\boldsymbol{F}^p, \bar{\epsilon}^p, T) + W^h(T), \tag{20}$$

where $J = \det \boldsymbol{F}$ is the Jacobian, $W^{e,vol}$ and $W^{e,dev}$ determine the volumetric and deviatoric thermoelastic response of the material upon unloading, whereas W^p represents the stored energy due to the plastic working of the material and W^h describes the heat storage capacity. The forms of $W^{e,vol}$, $W^{e,dev}$ and W^p depend on the specific material models. For instance, at extreme dynamic events, the elastic deviatoric response of the material is assumed to be quadratic in the elastic logarithmic strains, with isotropic elastic coefficients depending on temperature and vanishing beyond the melting temperature:

$$W^{e,dev}(\boldsymbol{F}\boldsymbol{F}^{p-1}, T) = \mu(J, T)\boldsymbol{\varepsilon}^{\mathrm{e,\ dev}} : \boldsymbol{\varepsilon}^{\mathrm{e,\ dev}} \tag{21}$$

where μ is the shear modulus of the material and $\boldsymbol{\varepsilon}^{\mathrm{e,\ dev}}$ represents the deviatoric elastic strain tensor in linearized kinematics by using the logarithmic mapping from finite to linearized kinematics [61,62], i.e.,

$$\boldsymbol{\varepsilon}^{\mathrm{e,\ dev}} = \frac{1}{2}\log(J^{-\frac{2}{3}}\mathbf{F}^{eT}\mathbf{F}^e). \tag{22}$$

The volumetric material response in the high pressure and temperature regime is governed by an Equation of State (EoS). In our numerical analyses, we use the SESAME EoS database [63] to compute pressure and free energy as a function of temperature and volumetric deformation in all the solid, liquid and gas phases. Additionally, the commonly used isotropic hardening model assumes a power-law form for the plastic work dependent solely on $\bar{\epsilon}^p$,

$$W^p(\boldsymbol{F}^p, \bar{\epsilon}^p, T) = \frac{n\sigma_y(T)\bar{\epsilon}_0^p}{n+1}\left(1 + \frac{\bar{\epsilon}^p}{\bar{\epsilon}_0^p}\right)^{\frac{n+1}{n}}, \tag{23}$$

where $\bar{\epsilon}_0^p$ is the reference effective plastic strain and $n > 1$ is the hardening exponent. σ_y is the initial yield stress as a function of temperature given by

$$\sigma_y(T) = \begin{cases} \sigma_0 \left(1 - \frac{T-T_0}{T_m-T_0}\right)^l & \text{if } T < T_m \\ 0 & \text{otherwise} \end{cases} \tag{24}$$

where T_0, T_m, σ_0 and l are the reference and melting temperature, the initial quasistatic yield stress at the absolute zero temperature and the softening exponent, respectively. Note that there is no back-stress due to kinematic hardening in this model, the plastic work vanishes and the plastic strains have been relaxed once the local temperature reaches the melting temperature. Consequently, as the material point melts or vaporizes, the local Helmholtz free energy density automatically changes to be of the simple form

$$A = W^{e,vol}(J, T) + W^h(T), \tag{25}$$

which represents the response of the liquid or gas phase as long as an appropriate EoS is employed. The heat capacity part of the free energy is generally a concave function of temperature. For example, the classical expression of W^h can be stated as

$$W^h(T) = C(T)\left(T - T_0 - T\log\frac{T}{T_0}\right), \tag{26}$$

where $C(T)$ is the temperature-dependent specific heat capacity coefficient per unit undeformed volume. To account for the phase transition, we assume there is a temperature window (also called the mushy zone), $T \in [T_p - \Delta T, T_p + \Delta T]$ where T_p is the phase change temperature, within which the material changes from one phase to the other gradually. A phase transition function introduced to describe the smooth transition between two phases is of the form

$$\alpha(T) = \frac{1}{2}\left[1 + \mathrm{erf}\left(\frac{T - T_p}{\sqrt{2}\sigma}\right)\right], \tag{27}$$

and its derivative with respect to temperature can be stated as

$$\frac{\mathrm{d}\alpha}{\mathrm{d}T} = \frac{1}{\sqrt{2\pi}\sigma}\exp\left[-\frac{(T - T_p)^2}{2\sigma^2}\right], \tag{28}$$

where σ is the standard deviation of the transition zone interval. Furthermore, we employ the apparent heat capacity method to take into consideration the effect of the latent heat by increasing the heat capacity of the material in the temperature window [64]. Thus, the heat capacity is stated as a function of temperature and phase transition function as

$$C(T) = C_{\text{phase1}}(1 - \alpha(T)) + C_{\text{phase2}}\alpha(T) + \rho_0 L\frac{\mathrm{d}\alpha}{\mathrm{d}T}, \tag{29}$$

where L denotes the latent heat during the phase transition, C_{phase1} and C_{phase2} are the heat capacity coefficient of phase 1 and 2, respectively.

Therefore, the Helmholtz free energy density concerning multiphase transition is of the form

$$\begin{aligned} A(\boldsymbol{F}, \boldsymbol{Z}, T) = {} & W^{\text{e, vol}}(J, T) + \mu(J, T)\boldsymbol{\varepsilon}^{\text{e, dev}} : \boldsymbol{\varepsilon}^{\text{e, dev}} \\ & + \frac{n\sigma_0(T)\bar{\epsilon}_0^p}{n+1}\left(1 + \frac{\bar{\epsilon}^p}{\bar{\epsilon}_0^p}\right)^{\frac{n+1}{n}} + C(T)\left(T - T_0 - T\log\frac{T}{T_0}\right). \end{aligned} \tag{30}$$

On the other hand, the viscous dissipation potential for weakly compressible Newtonian fluid can be stated as a function of the rate of deformation tensor $\boldsymbol{d}$ as

$$\phi^* = \eta(T) J \boldsymbol{d}^{\text{dev}} : \boldsymbol{d}^{\text{dev}}, \tag{31}$$

$$\boldsymbol{d} = \mathrm{sym}(\dot{\boldsymbol{F}}\boldsymbol{F}^{-1}), \tag{32}$$

where η is the temperature-dependent shear viscous coefficient, and $\boldsymbol{d}^{\text{dev}}$ the deviatoric part of $\boldsymbol{d}$. The viscous stress can also be derived from the viscous potential

$$\boldsymbol{P}^v = \frac{\partial \phi^*}{\partial \dot{\boldsymbol{F}}} = J\boldsymbol{\sigma}^v\boldsymbol{F}^{-T}, \tag{33}$$

where

$$\boldsymbol{\sigma}^{v} = 2\eta(T)\boldsymbol{d}^{\text{dev}} \tag{34}$$

is the viscous part of the Cauchy stress tensor. Thus, the first Piola–Kirchhoff stress tensor can be obtained as

$$\boldsymbol{P} = J\left(p(J,T)\boldsymbol{I} + 2\mu(T)\boldsymbol{\varepsilon}^{\text{e, dev}} + 2\eta(T)\boldsymbol{d}^{\text{dev}}\right)\boldsymbol{F}^{-T}. \tag{35}$$

where the pressure is computed from the EoS, $p(J,T) = \partial W^{\text{e, vol}}/\partial J$. Meanwhile, the heat generated by viscous dissipation takes the form

$$D_{int}^{v} = \boldsymbol{P}^{v} : \dot{\boldsymbol{F}}. \tag{36}$$

We further assume power-law rate-sensitivity. The corresponding dual kinetic potential is

$$\psi^{*} = \frac{m\sigma_y(T)\dot{\bar{\epsilon}}_0^p}{m+1}\left(1+\frac{\bar{\epsilon}^p}{\bar{\epsilon}_0^p}\right)^{\frac{1}{n}}\left(\frac{\dot{\bar{\epsilon}}^p}{\dot{\bar{\epsilon}}_0^p}\right)^{\frac{m+1}{m}} \tag{37}$$

where $m > 1$ is the rate-sensitivity exponent, $\dot{\bar{\epsilon}}^p$ and $\dot{\bar{\epsilon}}_0^p$ are the effective plastic strain rate and a reference plastic strain rate, respectively. The thermodynamic force conjugate to the internal variable, $\bar{\epsilon}^p$, is given by

$$Y = Y^{e} + Y^{d} = \frac{\partial W^{\text{e, dev}}}{\partial \bar{\epsilon}^p} + \frac{\partial W^{p}}{\partial \bar{\epsilon}^p} + \frac{\partial \psi^{*}}{\partial \dot{\bar{\epsilon}}^p} \equiv \sigma_c - \bar{\sigma} \tag{38}$$

where

$$\bar{\sigma} = \left(\boldsymbol{F}^{eT}\frac{\partial W^{\text{e, dev}}}{\partial \boldsymbol{F}^{e}}\right) : \boldsymbol{M} \tag{39}$$

is the effective von-Mises stress and

$$\sigma_c = \frac{\partial W^{p}}{\partial \bar{\epsilon}^p} + \frac{\partial \psi^{*}}{\partial \dot{\bar{\epsilon}}^p} = \sigma_0\left(1+\frac{\bar{\epsilon}^p}{\bar{\epsilon}_0^p}\right)^{\frac{1}{n}}\left[1+\left(\frac{\dot{\bar{\epsilon}}^p}{\dot{\bar{\epsilon}}_0^p}\right)^{\frac{1}{m}}\right]\left(1-\frac{T-T_0}{T_m-T_0}\right)^{l} \tag{40}$$

is the flow stress with strain hardening, rate-sensitivity and thermal softening. The heat generation due to the plastic dissipation can be estimated as [56]

$$D_{int}^{p} = Y^{d}\dot{\bar{\epsilon}}^p. \tag{41}$$

Finally, the dissipation due to heat conduction is assumed to follow the Fourier potential [65]

$$\chi(\boldsymbol{G};\boldsymbol{F},\boldsymbol{Z},T) = \frac{1}{2}\kappa(T)T\boldsymbol{G}^{2}, \tag{42}$$

and the Fourier heat flux is

$$\boldsymbol{q} = \frac{\partial \chi}{\partial \boldsymbol{G}} = \kappa(T)T\boldsymbol{G} = -\kappa(T)\nabla_0 T \tag{43}$$

where

$$\kappa(T) = \kappa_{phase1}(1-\alpha(T)) - \kappa_{phase2}\alpha(T) \tag{44}$$

is the heat conductivity coefficient as a function of temperature through the phase transition function $\alpha(T)$.

To summarize, the total dissipation potential of a thermoviscoplastic material at finite deformation involving phase transition is defined as

$$\Delta(\dot{\boldsymbol{F}},\dot{\bar{\epsilon}}^p,\boldsymbol{G}) = \eta(T)J\boldsymbol{d}^{\text{dev}} : \boldsymbol{d}^{\text{dev}} + \frac{m\sigma_y(T)\dot{\bar{\epsilon}}^p}{m+1}\left(1+\frac{\bar{\epsilon}_0^p}{\bar{\epsilon}_0^p}\right)^{\frac{1}{n}}\left(\frac{\dot{\bar{\epsilon}}^p}{\dot{\bar{\epsilon}}_0^p}\right)^{\frac{m+1}{m}} - \frac{1}{2}\kappa(T)T\boldsymbol{G}^{2}. \tag{45}$$

While the specific constitutive model assumes Newtonian viscosity and isotropic hardening laws, it is readily extensible to describe more complex internal dissipation mechanisms by introducing dedicated models for each term in Eq. (14), such as non-Newtonian viscosity, kinematic hardening and non-Fourier heat conduction laws. However,

the particular choices of the constitutive models in the decomposed Helmholtz free energy and dissipation potential lead to minor changes in the following numerical scheme.

2.2. Governing equations

The motion, deformation, temperature field and local state of a material system can be determined by solving the conservation and balance laws in the Lagrangian configuration. Based on the local thermomechanical model, the governing equations in the reference configuration include:
the conservation of mass

$$(\rho \circ \boldsymbol{\varphi}(\boldsymbol{X}, t))J = \rho_0, \tag{46}$$

the conservation of linear momentum,

$$\rho_0 \ddot{\boldsymbol{\varphi}} = \nabla_0 \boldsymbol{P} + \rho_0 \boldsymbol{B}, \tag{47}$$

the conservation of angular momentum,

$$\boldsymbol{P}\boldsymbol{F}^T = \boldsymbol{F}\boldsymbol{P}^T, \tag{48}$$

and the conservation of energy,

$$T\dot{N} = \boldsymbol{P}^v : \dot{\boldsymbol{F}} + \boldsymbol{Y}^d \cdot \dot{\boldsymbol{Z}} - \nabla \cdot \boldsymbol{q} + \rho_0 Q, \tag{49}$$

where ρ_0 is the density in the reference configuration, $\boldsymbol{B}$ is the body force per unit mass, and Q is the distributed heat source density per unit mass. Meanwhile, by introducing the dissipation potential Δ due to the internal processes and heat conduction, the second law of thermodynamics is satisfied automatically.

Besides the governing equations, the material system should also obey the boundary conditions in the Lagrangian form, i.e.

$$\boldsymbol{\varphi}(\boldsymbol{X}, t) = \bar{\boldsymbol{\varphi}}(\boldsymbol{X}, t) \quad \text{on } \Gamma_u \times [t_0, t] \tag{50}$$

$$\boldsymbol{P} \cdot \hat{\boldsymbol{N}} = \bar{\mathbf{T}} \quad \text{on } \Gamma_t \times [t_0, t] \tag{51}$$

$$T(\boldsymbol{X}, t) = \bar{T}(\boldsymbol{X}, t) \quad \text{on } \Gamma_T \times [t_0, t] \tag{52}$$

$$\bar{h} = \boldsymbol{q} \cdot \hat{\boldsymbol{N}} \quad \text{on } \Gamma_q \times [t_0, t] \tag{53}$$

where $\hat{\boldsymbol{N}}$ is the outward normal direction, $\bar{\boldsymbol{\varphi}}$, $\bar{\mathbf{T}}$, $\bar{T}$ and $\bar{h}$ are the applied displacement, traction, temperature and outward heat flux on the boundaries, respectively. The boundary of domain Ω_0 is defined as $\partial\Omega_0 = \Gamma_t \cup \Gamma_u = \Gamma_T \cup \Gamma_q$, where Γ_t is the Neumann boundary, Γ_u the Dirichlet boundary, Γ_T the temperature boundary, and Γ_q is the heat flux boundary.

2.3. Variational formulation

Based on the local thermomechanical model and the governing equations, we will extend the variational framework proposed by Yang [53] by including the inertial terms. To this end, the variational formulation describes the energy rate of the material system in general thermomechanical process is defined as

$$\begin{aligned}\Phi[\dot{\boldsymbol{\varphi}}, T, \dot{\boldsymbol{Z}}] = &\int_{\Omega_0} (\dot{K} + \dot{\mathcal{W}}) \mathrm{d}V - \int_{\Omega_0} \rho_0 \boldsymbol{B} \cdot \dot{\boldsymbol{\varphi}} \mathrm{d}V - \int_{\Gamma_t} \bar{\mathbf{T}} \cdot \dot{\boldsymbol{\varphi}} \mathrm{d}A \\ &+ \int_{\Omega_0} \rho_0 Q(t) \log \frac{T}{T_0} \mathrm{d}V - \int_{\Gamma_q} \bar{h}(t) \log \frac{T}{T_0} \mathrm{d}A,\end{aligned} \tag{54}$$

and the effective energy density $\mathcal{W}$ takes the form

$$\begin{aligned}\dot{\mathcal{W}} &= \dot{A} + N\dot{T} + \Delta(\frac{T}{\Theta}\dot{\boldsymbol{F}}, \frac{T}{\Theta}\dot{\boldsymbol{Z}}, \boldsymbol{G}) \\ &= \dot{A} + N\dot{T} + \phi^*(\frac{T}{\Theta}\dot{\boldsymbol{F}}) + \psi^*(\frac{T}{\Theta}\dot{\boldsymbol{Z}}) - \chi(\boldsymbol{G}),\end{aligned} \tag{55}$$

where K is the kinetic energy density. The state function $\Theta(\boldsymbol{F}, T, \boldsymbol{Z}) = \partial U/\partial N$ is derived from the internal energy, which can be treated as the internal temperature field, while T is the external temperature field. In thermal equilibrium conditions, $\Theta = T$ [53].

This variational formulation is suitable for general dissipative thermomechanical coupling problems including finite elastic and plastic deformation, rate-dependency, arbitrary flow and hardening rules. The linear momentum and energy conservation equations can be obtained as the Euler–Lagrangian equations of the functional Φ. Thus, the solutions $\{\dot{\boldsymbol{\varphi}}, \dot{T}, \dot{\boldsymbol{Z}}\}$ of the rate problem can be obtained from the stationarity conditions of the variational principle, such that

$$\inf_{\dot{\boldsymbol{\varphi}}} \sup_{T} \inf_{\dot{\boldsymbol{Z}}} \Phi[\dot{\boldsymbol{\varphi}}, \dot{T}, \dot{\boldsymbol{Z}}] \tag{56}$$

2.4. Time discretization

The time-dependent variational framework in Eq. (54) can be reduced to a sequence of incremental problems characterized by an optimization principle. For a given time increment $[t_n, t_{n+1}]$, if the state variables $\{\boldsymbol{\varphi_n}, T_n, \boldsymbol{Z_n}\}$ at time t_n are known, the approximation of state variables $\{\boldsymbol{\varphi_{n+1}}, T_{n+1}, \boldsymbol{Z_{n+1}}\}$ at time t_{n+1} may be obtained through minimization of the incremental energy, which is defined as the minimum of all admissible paths joining $\{\boldsymbol{\varphi_n}, T_n, \boldsymbol{Z_n}\}$ to $\{\boldsymbol{\varphi_{n+1}}, T_{n+1}, \boldsymbol{Z_{n+1}}\}$, i.e.

$$\Phi_n[\boldsymbol{\varphi_{n+1}}, T_{n+1}, \boldsymbol{Z_{n+1}}] = \inf_{\text{paths}} \int_{t_n}^{t_{n+1}} \Phi[\dot{\boldsymbol{\varphi}}, \dot{T}, \dot{\boldsymbol{Z}}]\mathrm{d}t. \tag{57}$$

Following the variational constitutive update in [53], the incremental effective energy density from t_n to t_{n+1} takes the form

$$\begin{aligned} \mathcal{W}^*_{n+1} - \mathcal{W}_n = {} & (t_{n+1} - t_n)\phi^*\left(\frac{T_{n+1}}{T_n}\frac{\Delta \boldsymbol{F}}{\Delta t}\right) - \chi(\boldsymbol{G}_{n+1}) + \chi(\boldsymbol{G}_n) \\ & + \inf_{\boldsymbol{Z}_{n+1}} \Big\{ N_n(T_{n+1} - T_n) + A(\boldsymbol{F}_{n+1}, \boldsymbol{Z}_{n+1}, T_{n+1}) \\ & - A(\boldsymbol{F}_n, \boldsymbol{Z}_n, T_n) + (t_{n+1} - t_n)\psi^*\left(\frac{T_{n+1}}{T_n}\frac{\Delta \boldsymbol{Z}}{\Delta t}\right) \Big\}, \end{aligned} \tag{58}$$

where we assume the state variables $\boldsymbol{\varphi_{n+1}}, T_{n+1}, \boldsymbol{Z_{n+1}}$ are independent. It is noteworthy that the incremental functional Φ_n does not involve the gradient of the internal variables $\boldsymbol{Z}_{n+1}$. As a result, the internal variables can be solved by taking extrema of related terms in the incremental variational potential. The effective energy density reduces to

$$\mathcal{W}^*(\boldsymbol{\varphi_{n+1}}, T_{n+1}) = \mathcal{W}(\boldsymbol{\varphi_{n+1}}, T_{n+1}, \boldsymbol{Z^*_{n+1}}) \tag{59}$$

where

$$\boldsymbol{Z^*_{n+1}} = \arg \inf_{\boldsymbol{Z}_{n+1}} \left\{ N_n(T_{n+1} - T_n) + A_{n+1} - A_n + (t_{n+1} - t_n)\psi^* \right\} \tag{60}$$

Note that with the complex temperature dependence of ϕ^* and ψ^*, special precautions must be taken in approximating the time integral. Consistent incremental approximation of dissipation can be found in [55].

A number of approaches for time discretization of the kinetic energy is presented in [66]. In this work, the Optimal Transportation Theory is introduced as a specific time discretization scheme for the kinetic energy within the incremental framework [38]. Thus, the exact minimum of the incremental kinetic energy in time interval $[t_n, t_{n+1}]$ can be expressed as the Wasserstein distance between the initial and final mass densities [48], i.e.,

$$d^2_W(\rho_n, \rho_{n+1}) = \inf_{\text{paths}} \{(t_{n+1} - t_n) \int_{t_n}^{t_{n+1}} \int_{\Omega_n} \rho_n |\dot{\boldsymbol{\varphi}}|^2 \mathrm{d}V\,\mathrm{d}t\} \tag{61}$$

where the Wasserstein distance is defined as

$$d^2_W(\rho_n, \rho_{n+1}) = \inf_{T} \int_{\Omega_n} |T(\boldsymbol{x}) - \boldsymbol{x}|^2 \rho_n(\boldsymbol{x})\mathrm{d}V \tag{62}$$

and T is any admissible map transporting ρ_n to ρ_{n+1}. Considering the backward Euler approximation for the time discretization of all the other terms in Eq. (54), the semi-discretized incremental variational formulation may be obtained as

$$\begin{aligned}\mathcal{I}_n[\boldsymbol{\varphi_{n+1}}, T_{n+1}] = &\frac{1}{2}\frac{d_W^2(\rho_n, \rho_{n+1})}{\Delta t} + \int_{\Omega_n}(\mathcal{W}^*_{n+1} - \mathcal{W}_n)\mathrm{d}V \\ &- \int_{\Omega_n}\rho_n \boldsymbol{B}_{n+1}\cdot\Delta\boldsymbol{\varphi}\mathrm{d}V - \int_{\Gamma_t}\bar{\mathbf{T}}_{n+1}\cdot\Delta\boldsymbol{\varphi}\mathrm{d}A \\ &+ \int_{\Omega_n}\rho_n Q_{n+1}\log\frac{T_{n+1}}{T_n}\Delta t\mathrm{d}V - \int_{\Gamma_q}\bar{h}_{n+1}\log\frac{T_{n+1}}{T_n}\Delta t\mathrm{d}A.\end{aligned} \tag{63}$$

Taking variations of $\mathcal{I}_n$ and applying the local thermodynamic models (6)–(11), (36) and (41), one has

$$\begin{aligned}\langle\delta\mathcal{I}_n, \delta\boldsymbol{\varphi}_{n+1}\rangle = &\int_{\Omega_n}\frac{2\rho_n}{\Delta t}\left(\frac{\boldsymbol{\varphi}_{n\to n+1}(\boldsymbol{x}) - \boldsymbol{x}}{\Delta t} + \frac{\boldsymbol{\varphi}^{-1}_{n-1\to n}(\boldsymbol{x}) - \boldsymbol{x}}{\Delta t}\right)\cdot\delta\boldsymbol{\varphi}_{n+1}\mathrm{d}V \\ &+ \int_{\Omega_n}(\boldsymbol{P}^e_{n+1} + \boldsymbol{P}^v_{n+1}) : \delta\boldsymbol{F}_{n+1}\mathrm{d}V \\ &- \int_{\Omega_n}\rho_n\boldsymbol{B}_{n+1}\cdot\delta\boldsymbol{\varphi}_{n+1}\mathrm{d}V - \int_{\Gamma_t}\bar{\mathbf{T}}_{n+1}\cdot\delta\boldsymbol{\varphi}_{n+1}\mathrm{d}V,\end{aligned} \tag{64}$$

and

$$\begin{aligned}\langle\delta\mathcal{I}_n, \delta T_{n+1}\rangle = &\Delta t\left\{\int_{\Omega_n}\left[\frac{N_n - N_{n+1}}{\Delta t}\delta T_{n+1} + \boldsymbol{P}^v_{n+1} : \dot{\boldsymbol{F}}_{n+1}\frac{\delta T_{n+1}}{T_n}\right.\right. \\ &\left.+\boldsymbol{Y}^d_{n+1}\cdot\dot{\boldsymbol{Z}}_{n+1}\frac{\delta T_{n+1}}{T_n} - \boldsymbol{q}_{n+1}\cdot\delta\boldsymbol{G}_{n+1}\right]\mathrm{d}V \\ &\left.+\int_{\Omega_n}\rho_n Q_{n+1}\frac{\delta T_{n+1}}{T_{n+1}}\mathrm{d}V - \int_{\Gamma_q}\bar{h}_{n+1}\frac{\delta T_{n+1}}{T_{n+1}}\mathrm{d}A\right\},\end{aligned} \tag{65}$$

where the minimizer of the incremental action is given in terms of McCann's displacement interpolation [67],

$$\boldsymbol{\varphi}(\boldsymbol{x}, t) = \frac{t_{n+1} - t}{t_{n+1} - t_n}\boldsymbol{x} + \frac{t - t_n}{t_{n+1} - t_n}\boldsymbol{\varphi}_{n\to n+1}(\boldsymbol{x}), \tag{66}$$

and

$$\dot{\boldsymbol{\varphi}}(\boldsymbol{x}, t) = \frac{\boldsymbol{\varphi}_{n\to n+1}(\boldsymbol{x}) - \boldsymbol{x}}{t_{n+1} - t_n}. \tag{67}$$

Enforcing stationarity, i.e., $\delta\mathcal{I}_n = 0$, yields the semi-discretized linear momentum conservation and energy conservation equations in the time interval $[t_n, t_{n+1}]$ as well as the Neumann boundary conditions. Then, the evolution of the deformation and temperature field is identified with the sequence of extrema of the reduced incremental potential:

$$\inf_{\boldsymbol{\varphi_{n+1}}}\sup_{T_{n+1}}\mathcal{I}_n[\boldsymbol{\varphi_{n+1}}, T_{n+1}]. \tag{68}$$

2.5. Spatial discretization

Next, we proceed to the spatial discretization of the computational domain for the numerical approximation of the variations of the incremental potential. The space $\mathcal{V}$ of admissible thermo-mechanical configurations at time t is given by

$$\begin{aligned}\mathcal{V} = \{&\boldsymbol{\varphi} : \Omega_0 \to \Re^3 \mid \boldsymbol{\varphi} = \bar{\boldsymbol{\varphi}}(t) \text{ on } \Gamma_u, \nabla_0\boldsymbol{\varphi} \in \mathrm{GL}^+(3, \Re); \\ &T : \Omega_0 \to \Re^+ \mid T = \bar{T}(t) \text{ on } \Gamma_T\}.\end{aligned} \tag{69}$$

A standard Ritz–Galerkin approach is considered to construct the admissible subspace $\mathcal{V}^h$ on a given spatial discretization $\mathcal{T}^h$ with N number of nodes as an approximation to $\mathcal{V}$

$$\begin{aligned}\mathcal{V}^h = \{\boldsymbol{\varphi}^h : \Omega_0 \times [t_0, t] \to \Re^3 \mid \boldsymbol{\varphi}^h(\boldsymbol{X}, t) = \sum_{a=1}^{N} \boldsymbol{x}_a(t) N_a(\boldsymbol{X});\\ T^h : \Omega_0 \times [t_0, t] \to \Re^+ \mid T^h(\boldsymbol{X}, t) = \sum_{a=1}^{N} T_a(t) N_a(\boldsymbol{X})\},\end{aligned} \tag{70}$$

where $\boldsymbol{x}_a = \boldsymbol{\varphi}(\boldsymbol{X}_a, t)$ and $T_a = T(\boldsymbol{X}_a, t)$ are the current coordinates and temperatures of a node a in the node set $\mathcal{M}_0 = \{\boldsymbol{X}_a, a = 1, \ldots, N\}$, N_a is the shape function associated with node $\boldsymbol{x}_a$ at time t. The discrete deformation and temperature gradient are approximated as

$$\boldsymbol{F}^h(\boldsymbol{X}, t) = \sum_{a=1}^{N} \boldsymbol{x}_a(t) \otimes \nabla_0 N_a(\boldsymbol{X}) \tag{71}$$

$$\boldsymbol{G}^h(\boldsymbol{X}, t) = -\frac{\sum_{b=1}^{N} T_b(t) \nabla_0 N_b(\boldsymbol{X})}{\sum_{a=1}^{N} T_a(t) N_a(\boldsymbol{X})} \tag{72}$$

In order to account for large deformations in materials under extreme thermomechanical conditions, the Local Maximum Entropy (LME) approximation scheme is employed to construct the shape functions for displacement and temperature fields [49]. The LME shape functions provide a variety of advantages for the meshfree approximation of functions, such as automatic satisfaction of the zero- and first-order consistency, non-negativity, weak Kronecker-Delta property, and robust and efficient solution scheme, etc [68]. Within the incremental formulation, the configuration mapping $\boldsymbol{\varphi}_{n\to n+1}$ from time t_n to t_{n+1} and the current temperature can be obtained as

$$\boldsymbol{x}_{n+1} = \boldsymbol{\varphi}_{n\to n+1}(\boldsymbol{x}_n) = \sum_{a\in\mathcal{A}} \boldsymbol{x}_{a,n+1} N_a(\boldsymbol{x}_n), \tag{73}$$

$$T_{n+1}(\boldsymbol{x}) = \sum_{a\in\mathcal{A}} T_{a,n+1} N_a(\boldsymbol{x}_n), \tag{74}$$

where $\boldsymbol{x}_{a,n+1}$ and $T_{a,n+1}$ are the coordinates and temperature of node $\boldsymbol{x}_a$ at time t_{n+1}, respectively. $\mathcal{A}$ is an index set for nodes in $N_H(\boldsymbol{x}_n) \equiv \{\boldsymbol{x}_{a,n} \in \mathcal{M}_n :\| \boldsymbol{x}_n - \boldsymbol{x}_{a,n} \| \leq h_{a,n}\}$, i.e., a set of nodes whose support of the shape function covers the location $\boldsymbol{x}_n$ or the neighborhood of a point $\boldsymbol{x}$ at time t_n. LME approximants have a Gaussian decay that is modulated by a non-dimensional parameter γ, which controls the effective support of the resulting shape functions as $h_a = h\sqrt{-\log(\delta_0)\gamma_a}$, where h is the nodal spacing and δ_0 is a cutoff-tolerance below which the shape functions are considered to vanish. Note that the neighborhood $N_H(\boldsymbol{x}_n)$ is redefined on-the-fly during the computation in the deformed configuration at time t_n based on the current support size $h_{a,n}$ of node $\boldsymbol{x}_a$ and the shape functions $N_a(\boldsymbol{x}_n)$ must be recalculated as the neighborhood varies. For an isotropic support, the support size can be updated according to the local volumetric deformation of the node, for instance, $h_{a,n} = h_{a,0}\sqrt[d]{\det \boldsymbol{F}_{a,n}}$.

To fully discretize the variations of the incremental actions, we begin by approximating the usual Lebesgue measure L of the volume at t_n by discrete measures of the form

$$L_n^h = \sum_{p=1}^{M} v_{p,n} \delta(\boldsymbol{x} - \boldsymbol{x}_{p,n}) \tag{75}$$

concentrated at material points $\boldsymbol{x}_{p,n}$, each of which is assigned a discrete volume $v_{p,n}$ at time t_n. The position, temperature, deformation and temperature gradient of the material point at time t_{n+1} are approximated by

$$\boldsymbol{x}_{p,n+1} = \sum_{a\in\mathcal{A}_p} \boldsymbol{x}_{a,n+1} N_a(\boldsymbol{x}_{p,n}), \tag{76}$$

$$T_{p,n+1} = \sum_{a\in\mathcal{A}_p} T_{a,n+1} N_a(\boldsymbol{x}_{p,n}), \tag{77}$$

$$\boldsymbol{F}_{p,n+1} = \sum_{a\in\mathcal{A}_p} \left[\boldsymbol{x}_{a,n+1} \otimes \nabla N_a(\boldsymbol{x}_{p,n})\right] \circ \boldsymbol{F}_{p,n}, \tag{78}$$

$$\boldsymbol{G}_{p,n+1} = -\frac{\sum_{a\in\mathcal{A}_p} T_{a,n+1}\nabla N_a(\boldsymbol{x}_{p,n})}{\sum_{a\in\mathcal{A}_p} T_{a,n+1} N_a(\boldsymbol{x}_{p,n})} \tag{79}$$

where $\mathcal{A}_p$ is the index set for nodes belonging to the neighborhood of $\boldsymbol{x}_{p,n}$. Variations of the incremental potential $\mathcal{I}_n$ in the approximation subspace $\mathcal{V}_h$ are now taken with respect to the nodal unknowns at time t_{n+1}. Applying the discrete measures to Eqs. (64) and (65), and enforcing stationarity conditions yield the fully discrete mechanical and thermal balance equations

$$\boldsymbol{f}^{int}_{a,n+1} - \boldsymbol{f}^{ext}_{a,n+1} = m_{a,n+1}\ddot{\boldsymbol{\varphi}}_{a,n+1}, \tag{80}$$

$$Q^{int}_{a,n+1} - Q^{ext}_{a,n+1} = 0, \tag{81}$$

where

$$m_{a,n+1} = \sum_{\boldsymbol{x}_{p,n}\in N_H(\boldsymbol{x}_{a,n})} m_p N_a(\boldsymbol{x}_{p,n}) \tag{82}$$

denotes the lumped mass from the material points to the node $\boldsymbol{x}_a$ at t_{n+1},

$$\ddot{\boldsymbol{\varphi}}_{a,n+1} = \frac{2}{t_{n+1}-t_{n-1}}\left(\frac{\boldsymbol{x}_{a,n+1}-\boldsymbol{x}_{a,n}}{t_{n+1}-t_n} - \frac{\boldsymbol{x}_{a,n}-\boldsymbol{x}_{a,n-1}}{t_n - t_{n-1}}\right) \tag{83}$$

is a central difference approximation of the nodal acceleration. In the balance equations, the internal nodal force is defined as

$$\boldsymbol{f}^{int}_{a,n+1} = \sum_{p\in N_H(\boldsymbol{x}_{a,n})} \left[\boldsymbol{P}^e(\boldsymbol{F}_{p,n+1}) + \boldsymbol{P}^v(\dot{\boldsymbol{F}}_{p,n+1})\right]\cdot\nabla N_a(\boldsymbol{x}_{p,n}) v_{p,n}, \tag{84}$$

$\boldsymbol{f}^{ext}_{a,n+1}$ denotes the external nodal force due to body forces and applied traction

$$\boldsymbol{f}^{ext}_{a,n+1} = \sum_{p\in N_H(\boldsymbol{x}_{a,n})} \rho_{p,n}\boldsymbol{B}_{p,n+1} N_a(\boldsymbol{x}_{p,n}) v_{p,n} + \sum_{q\in\Gamma_t(\boldsymbol{x}_{a,n})} \bar{\mathbf{T}}_{q,n+1} N_a(\boldsymbol{x}_{q,n}) A_{q,n}, \tag{85}$$

the internal and external nodal heat are given by

$$\begin{aligned} Q^{int}_{a,n+1} = \sum_{p\in N_H(\boldsymbol{x}_{a,n})} v_{p,n} \Big\{ & (N_{p,n} - N_{p,n+1}) N_a(\boldsymbol{x}_{p,n}) \\ & + \left[\boldsymbol{P}^v(\dot{\boldsymbol{F}}_{p,n+1}) : \Delta\boldsymbol{F}_{p,n} + \boldsymbol{Y}^d(\dot{\boldsymbol{Z}}_{p,n+1})\cdot\Delta\boldsymbol{Z}_{p,n}\right]\frac{N_a(\boldsymbol{x}_{p,n})}{T_{p,n}} \\ & + \frac{\Delta t}{T_{p,n+1}}\boldsymbol{q}(T_{p,n+1})\cdot\left[\nabla N_a(\boldsymbol{x}_{p,n}) + \boldsymbol{G}_{p,n+1} N_a(\boldsymbol{x}_{p,n})\right]\Big\}, \\ Q^{ext}_{a,n+1} = \sum_{q\in\Gamma_q(\boldsymbol{x}_{a,n})} & \Delta t \bar{h}_{q,n+1}\frac{N_a(\boldsymbol{x}_{q,n})}{T_{q,n+1}} A_{q,n} \\ & - \sum_{p\in N_H(\boldsymbol{x}_{a,n})} \Delta t \rho_{p,n} Q_{p,n+1}\frac{N_a(\boldsymbol{x}_{p,n})}{T_{p,n+1}} v_{p,n}, \end{aligned} \tag{86}$$

respectively, where $N_H(\boldsymbol{x}_{a,n})$ is the support of the LME shape function at node $\boldsymbol{x}_a$ at time t_n. In the calculations, a dynamic search algorithm based on the deformation-dependent geometrical information is essential to reconstruct the dynamic connectivity between the material points and nodes, which enables the computation framework to deal with problems involving large deformations. A schematic demonstration of the spatial discretization and reconstruction of the connectivity between the material points and nodes is shown in Fig. 1.

The solution techniques for the system of balance equations (80) and (81) can be categorized into two groups of time-stepping algorithms, i.e., simultaneous and split algorithms. In the simultaneous algorithms, mechanical and thermal balance equations are solved simultaneously either by an explicit or implicit method using the same time step. However, a fully explicit simultaneous method faces stability issues, and the well-known Courant–Friedrichs–Lewy (CFL) conditions restrict the time step size to be less than the transit time of a sound wave traveling through the smallest discretization. Nevertheless, the time scale for heat transfer can be much larger than the one required for the wave propagation in solids and fluids. Alternatively, a fully implicit method involves a very expensive calculation

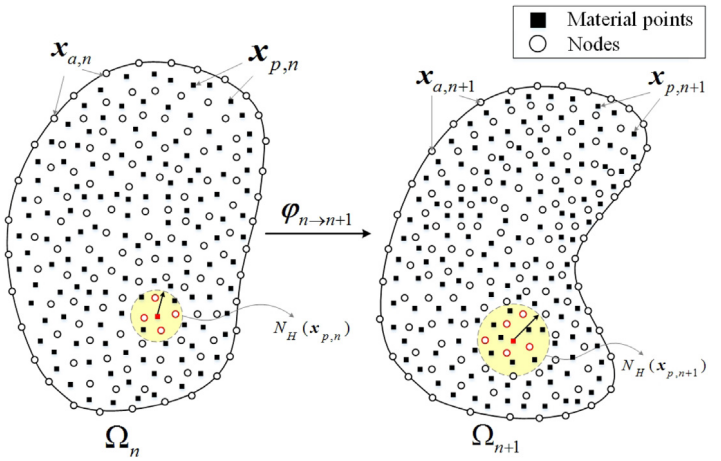

Fig. 1. Schematic of the HOTM approximation scheme.

of the tangent of the mechanical forces (a fourth-order tensor), which is further exacerbated in large scale three-dimensional simulations of materials with complex constitutive relations under extreme thermomechanical coupling conditions. Split algorithms take advantage of an operator split to decouple the solution procedure: mechanical balance equations and thermal balance equations are solved sequentially. In this work, an isothermal split algorithm is employed in which the mechanical balance equations at time t_{n+1} are solved at a constant temperature obtained at time t_n, while the thermal balance equations at time t_{n+1} are solved at the fixed deformed configuration Ω_{n+1}. Based on the temporal discretization of the potential, the mechanical balance equations (80) can be solved explicitly, while the thermal balance equations (81) solved by an implicit method. Specifically, the Newton–Raphson iterations are performed to find the solution of Eqs. (81). The proposed solution technique also falls into the framework of explicit–implicit methods. Table 1 outlines the general structure of the Hot Optimal Transportation Meshfree (OTM) method. Note that the time step for the two solvers can be different. In our numerical tests, we assume that the time step for thermal solver is an integral multiple of the time step for the mechanical solver.

3. Numerical results

3.1. Verification of the meshfree thermal solver: three-dimensional transient heat conduction problem

In this section, the accuracy and convergence of the meshfree solution of the thermal balance equations (81) are studied in a three-dimensional nonlinear transient heat conduction problem presented by Amar [69]. The performance of the meshfree mechanical solver can be found in the verification and validation tests of the OTM method [39]. Consider a cube with homogeneous material properties, whose center is at the origin and length is L, is embedded in gas with a constant temperature of T_r. Perfect gas convective boundary conditions are applied to all six faces, while the heat transfer coefficients are only the same on opposing surfaces. The problem can be stated as the following

$$\begin{cases} C\frac{\partial T}{\partial t} - \nabla\cdot(\kappa\nabla T) = 0 \\ k\nabla T\cdot\hat{n} = H_x(T_r - T) \text{ for } x = -L/2 \text{ and } x = L/2 \\ k\nabla T\cdot\hat{n} = H_y(T_r - T) \text{ for } y = -L/2 \text{ and } y = L/2 \\ k\nabla T\cdot\hat{n} = H_z(T_r - T) \text{ for } z = -L/2 \text{ and } z = L/2 \end{cases} \tag{87}$$

where the material parameters are listed in Table 2.

The analytical solution of Eqs. (87) can be obtained by combining the one-dimensional solution of the transient heat conduction equation with convective heat transfer boundary conditions [70]. The exact solution of the one-dimensional problem in x-direction presented by Arpaci in 1966 [71] is given by

$$\theta_x(x,t) = \frac{T(X,t) - T_r}{T_0 - T_r} = 2\sum_{n=1}^{\infty}\left(\frac{\sin\nu_n}{\nu_n + \sin\nu_n\cos\nu_n}\right)\exp(-\nu_n^2\alpha t/L^2)\cos(\nu_n x/L), \tag{88}$$

Table 1
The isothermal split algorithm.

Algorithm	
Step 1:	Set $n = 0$. Initialize nodal coordinates $\boldsymbol{x}_{a,n}$, material point position $\boldsymbol{x}_{p,n}$, volume $v_{p,n}$, density $\rho_{p,n}$, and neighborhood $N_H(\boldsymbol{x}_{p,n})$. Compute the shape function $N_a(\boldsymbol{x}_{p,n})$ and derivatives $\nabla N_a(\boldsymbol{x}_{p,n})$, and the deformation gradient $\boldsymbol{F}(\boldsymbol{x}_{p,n})$. Compute the lumped mass $m_{a,n}$, linear momenta $\boldsymbol{l}_{a,n}$ and nodal force $\boldsymbol{f}_{a,n}$
Step 2:	Update nodal coordinates: $\boldsymbol{x}_{a,n+1} = \boldsymbol{x}_{a,n} + (t_{n+1} - t_n) m_{a,n}^{-1} (\boldsymbol{l}_{a,n} + \frac{t_{n+1} - t_{n-1}}{2} \boldsymbol{f}_{a,n})$
Step 3:	Compute the deformation gradient: $\boldsymbol{F}_{p,n\to n+1} = \boldsymbol{x}_{a,n+1} \otimes \nabla N_a(\boldsymbol{x}_{p,n})$ $\boldsymbol{F}_{p,n+1} = \boldsymbol{F}_{p,n\to n+1} \circ \boldsymbol{F}_{p,n}$
Step 4:	Find the internal variables $\boldsymbol{Z}_{n+1}$ implicitly
Step 5:	Update the nodal forces, linear momenta and lumped mass: $\boldsymbol{f}_{a,n+1} = \boldsymbol{f}_{a,n+1}^{int} - \boldsymbol{f}_{a,n+1}^{ext}$ $\boldsymbol{l}_{a,n+1} = \boldsymbol{l}_{a,n} + \frac{1}{2}(\boldsymbol{f}_{a,n+1} - \boldsymbol{f}_{a,n})(t_{n+1} - t_n)$ $m_{a,n+1} = \sum_{p \in N_H(\boldsymbol{x}_{a,n})} m_p N_a(\boldsymbol{x}_{p,n})$.
Step 6:	If thermal solver is activated, find $T_{a,n+1}$: (i) Set $k = 0$, $T_{a,n+1}^{(k)} = T_{a,n}$ and tolerance $\epsilon \ll 1$ (ii) Compute $R_{a,n+1}^{(k)} = Q_{a,n+1}^{\mathrm{int}(k)} - Q_{a,n+1}^{\mathrm{ext}(k)}$ (ii) If $R_{a,n+1}^{(k)} > \epsilon$ calculate $\Delta T_{a,n+1}^{(k)} = \left(\frac{\mathrm{d}R_{a,n+1}^{(k)}}{\mathrm{d}T_{b,n+1}} \right)^{-1} R_{b,n+1}^{(k)}$ $T_{a,n+1}^{(k+1)} = T_{a,n+1}^{(k)} + \Delta T_{a,n+1}^{(k)}$ set $k \leftarrow k + 1$, go to (ii) Else $T_{a,n+1} = T_{a,n+1}^{(k)}$
Step 7:	Update the material point coordinates, neighborhood and volume: $\boldsymbol{x}_{p,n+1} = \sum_{a \in N_H(\boldsymbol{x}_{p,n})} \boldsymbol{x}_{a,n+1} N_a(\boldsymbol{x}_{p,n})$, $N_H(\boldsymbol{x}_{p,n+1}) = \{\boldsymbol{x}_{a,n+1} \text{ s.t. } \|\boldsymbol{x}_{a,n+1} - \boldsymbol{x}_{p,n+1}\| < h_{a,n+1}\}$, $v_{p,n+1} = \det(\boldsymbol{F}_{p,n\to n+1}) v_{p,n}$.
Step 8:	Recompute shape functions $N_a(\boldsymbol{x}_{p,n+1})$ and derivatives $\nabla N_a(\boldsymbol{x}_{p,n+1})$ from the updated neighborhood $N_H(\boldsymbol{x}_{p,n+1})$.
Step 9:	Reset $n = n + 1$. Go to Step 2 until the maximum number of iteration.

Table 2
Cube convection problem parameters.

$T_0 = 300$ K
$T_r = 1300$ K
$L = 0.01$ m
$C = 4 \times 10^6$ J/m^3
$k = 10$ W/m K
$\alpha = \kappa / C = 2.5 \times 10^{-6}$ m^2/s
$H_x = 1500$ W/m^2 K
$H_y = 1000$ W/m^2 K
$H_z = 500$ W/m^2 K

where the values of ν_n can be obtained by solving the equation

$$\nu_n \sin \nu_n = \mathrm{Bi} \cos \nu_n \quad \text{and} \quad \nu_n > 0, \tag{89}$$

and the Biot number Bi is defined as

$$\mathrm{Bi} = \frac{H_x L}{k}. \tag{90}$$

Likewise, the solutions θ_y in the y-direction and θ_z in z-direction follow the same expression. Thus, the analytical solution of the three dimensional problem can be written as

$$\frac{T(\boldsymbol{x}, t) - T_r}{T_0 - T_r} = \theta_x \theta_y \theta_z. \tag{91}$$

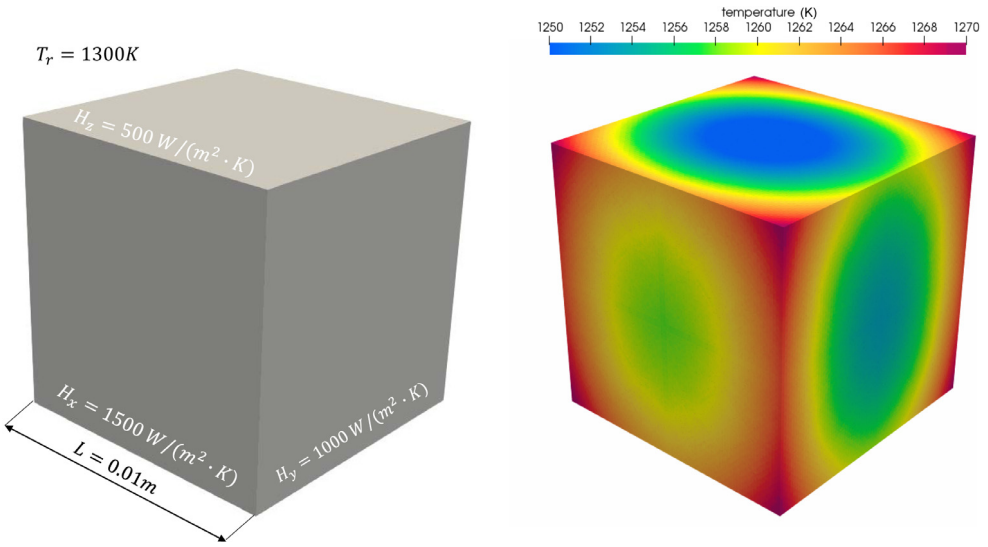

Fig. 2. Simulation solution at 25 s for cube convection problem.

Table 3
Mesh parameters.

	Number of degrees of freedom	Number of material points	Number of elements on each edge
Coarse	1711	8359	10
Medium	10 814	57 780	20
Fine	74 653	421 867	40
Very fine	596 240	3 368 680	80

Note that the above solution is valid only when $x \geq 0$, $y \geq 0$, and $z \geq 0$. Considering that the solution is symmetric across the $xy-$, $xz-$ and $yz-$ planes, the temperature field in the entire domain can be derived.

The problem is solved by the HOTM method assuming fixed configuration or no deformation. The computational domain is discretized by a tetrahedron mesh. We take the nodes of the mesh as the HOTM nodes and barycenters of the tetrahedra as the HOTM material points. The connectivity of the mesh is employed to build the initial neighborhood of the material points. Four tetrahedron meshes with the number of elements and degrees of freedom listed in Table 3 are tested. Fig. 2 shows the simulation result for the cube exposed in the gas for 25 s.

In the convergence tests, the normalized L^2 error of the temperature field is collected, i.e.,

$$L_2 = \sqrt{\frac{\int_\Omega \|T - \bar{T}\|^2 \mathrm{d}V}{\int_\Omega \|\bar{T}\|^2 \mathrm{d}V}}, \tag{92}$$

where T is the temperature at the nodes and $\bar{T}$ is the analytical solution calculated at each node based on Eq. (91). Fig. 3 shows the performance of the meshfree solver for the thermal balance equations. With the largest error less than 2×10^{-5} from the coarsest mesh, the numerical solutions show a second order convergence rate as the discretization size decreases.

3.2. Upsetting of a billet

This example is concerned with the application of the HOTM method for predicting materials dynamic behavior under extreme thermomechanical loading conditions arising from a typical forming process of metals. During the forming process, a metallic billet experiences a compression by a rigid piston, which usually results in a compression ratio beyond 65%. The extremely large deformation in the material causes a self-heating primarily induced by the plastic dissipation. Fig. 4 shows the initial experimental configuration and the predicted plastic strain distribution

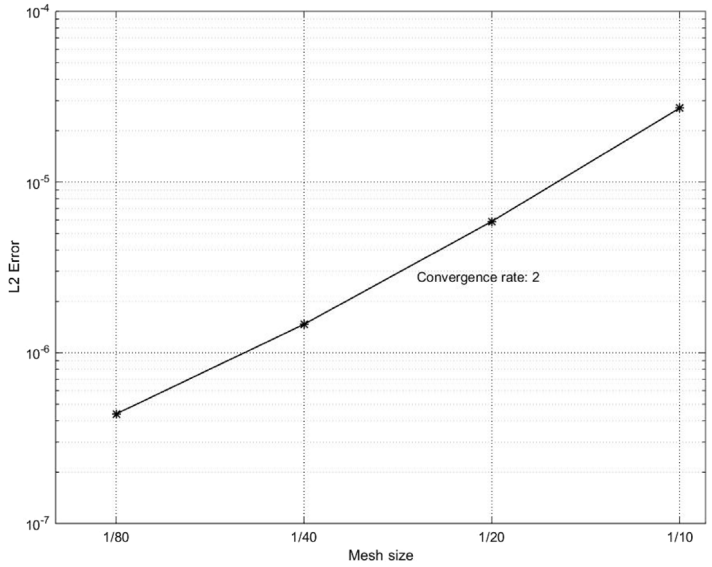

Fig. 3. Performance of the cube convection problem.

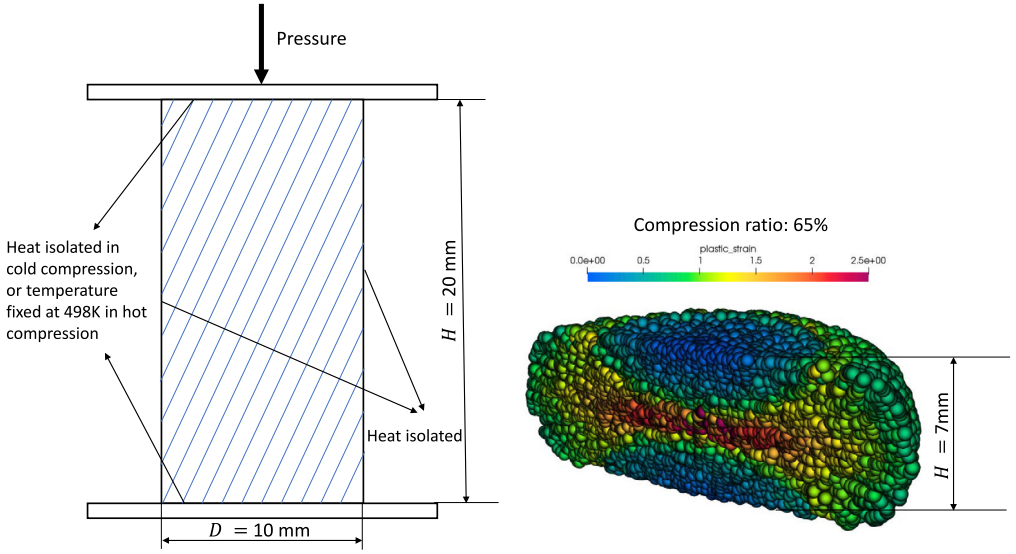

Fig. 4. Upsetting of a billet: The initial geometry and the plastic strain distribution at compression 65%.

in the deformed billet at the compression ratio of 65%. The complexity of the deformation mechanism is further compounded in case external heating or cooling strategies are applied to the surfaces of the billet. The accuracy and effectiveness of the HOTM method to address challenges in the simulation of extremely large deformation, strongly coupled thermomechanical response with general internal dissipation mechanisms are testified in the applications of cold, hot and adiabatic forming processes.

Simo et al. [8] conducted two-dimensional Finite Element analysis of upsetting a billet using the thermomechanical model of J_2 plastic flow theory with thermal softening. The billet was compressed by 64% in their tests which results in a temperature increase of 175 K at the center of the billet. The computational results presented in [8] may provide a benchmark test for comparing to the HOTM predictions of materials dynamic behavior under thermomechanical coupling conditions. Moreover, we extend the simulation by increasing the compression ratio beyond 90% in three dimensions under various thermal boundary conditions, which can postulate

Table 4
Material properties in the thermo-visco-plastic model.

Density ρ (kg/m^3)	2.7×10^3
Young's modulus E (Pa)	70×10^9
Poisson's ratio μ	0.33
Initial yield stress σ_0 (Pa)	2.0×10^8
Reference plastic strain ϵ_0^p	1.0×10^{-4}
Reference plastic strain rate $\dot{\epsilon}_0^p$	100 000
Rate sensitivity exponent m	0.001
Hardening exponent n	0.01
Reference temperature T_0 (K)	298
Melting temperature T_m (K)	925
Heat capacity C_v (J/(m^3 K))	2.42×10^6
Thermal softening exponent l	1.0

a scenario challenging to be solved by Lagrangian or Eulerian grid-based methods. In our tests, a cylindrical billet in the diameter of 10 mm and height of 20 mm is modeled by 39,568 material points and 38,684 degrees of freedom. The thermo-visco-plastic constitutive model presented in Section 2.1 is employed to describe the strong thermomechanical behavior of the material, where the material properties are listed in Table 4.

We consider two cases for the upsetting process with and without external heating mechanisms, namely, cold and hot compression. In both cases, a rigid piston compresses the billet at a constant velocity on the top surface with the non-slip condition to achieve the prescribed compression ratio, while the bottom surface is fixed. Fig. 5 shows the evolution of the temperature distribution at material points and the deformed configuration during the cold compression process, in which the billet has an initial temperature of 293 K and is isolated from the environment. The heat generated by the internal dissipation elevates the local temperature and is transferred to the entire cylinder through conduction. As the compression ratio increases to 91%, a significantly high plastic strain is developed in the body as shown in Fig. 6 and most of the material flow in the radial direction due to the constraint on the top and bottom surfaces. While the temperature continues to rise, the maximum temperature change is reached at the center of the cylinder by 400 K due to the highly localized plastic deformation.

Fig. 7 presents the simulation result of the hot compression process, where a fixed temperature of 498 K is applied to the top, and bottom surfaces and the cylindrical surface is isolated. At the beginning of the process, the billet is heated up and softened by the prescribed surface temperature. The heat transfer from the top/bottom surfaces towards the center and heat generation from the plastic dissipation by compression contribute to the evolution of the temperature field simultaneously. As the piston moves down, the temperature at the central part of the cylinder increases rapidly due to the localized plastic deformation. When the local temperature goes beyond 498 K, the heat flux flows from the center back to the boundary to rebalance the thermal field. In contrast to the cold compression test, the temperature raises gradually from the center to the boundary in the hot compression case. It is interesting that the maximum temperature increase found at the boundary at a compression ratio of 95% is 310 K, which is lower than the temperature jump in the cold compression test. At the end of the simulation, the height of the billet is only 5% of its original height as shown in Fig. 7, and the temperature is almost constant along the thickness direction. The extremely large deformation and strongly coupled thermomechanical response are noteworthy in the simulations.

Furthermore, the evolution of the temperature field at the center of the billet is recorded in both cases, as shown in Fig. 8. The temperature increases slowly during the cold compression comparing to the hot compression case, in which the inward heat flux from the boundary dominates the temperature change at the beginning of the process. However, the temperature raises drastically to 700 K as the material deforms intensively in the cold compression, while the temperature reaches a dynamic equilibrium around 510 K from compression ratio 40% to 95% during hot compression. The evolution of temperature predicted by the HOTM method in the cold compression case agrees very well with the results reported in Simo et al. [8]. The discrepancy may be a result of the difference in the form of the material model and constants.

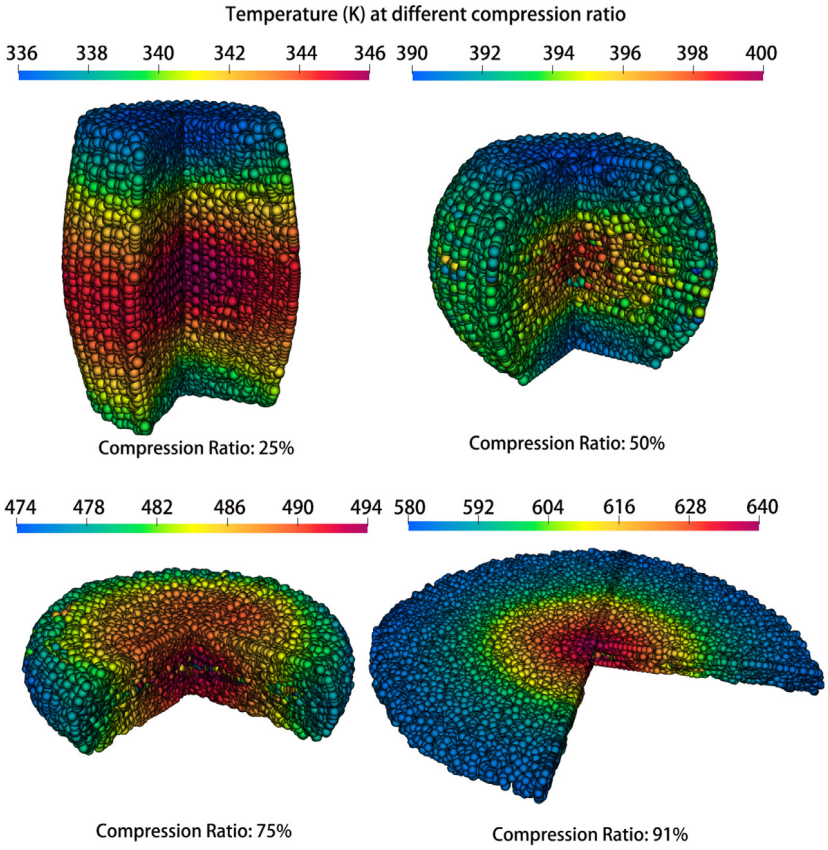

Fig. 5. HOTM simulation results of the cold compression case: evolution of the temperature field and deformed configuration at compression ratio 25%, 50%, 75% and 91%, with a maximum temperature increase of 400 K.

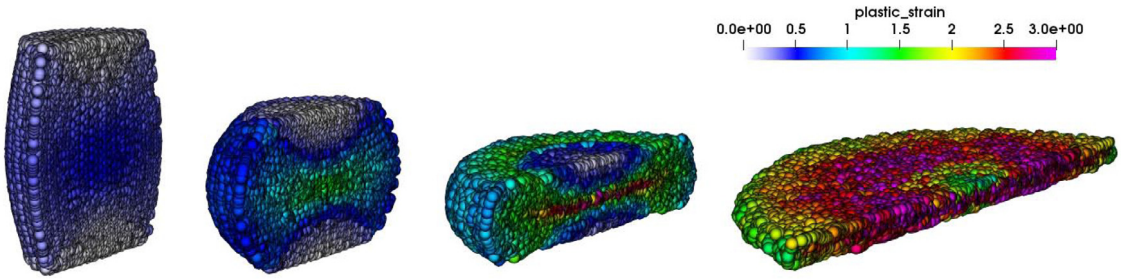

Fig. 6. HOTM simulation results of cold compression case: evolution of the plastic deformation in the billet at compression ratio 25%, 50%, 75% and 91% at the material points.

3.3. Application of the HOTM method for the laser cladding technology

Laser cladding technology has been widely applied in surface coating, rapid manufacturing and parts repair, in which a powder nozzle feeds a powdery additive into the laser zone to create a metal clad on the substrate [72]. Under the radiation of laser, the powder particles melt as they travel in air towards the substrate, while the substrate is partially irradiated to form a shallow melt pool on the surface. Since drops of liquid material merge into the substrate melt pool, the molten powder particles and the substrate fuse together nicely. When the substrate moves away from the laser zone, the melt pool solidifies to create a non-porous and metallurgically bonded layer. Fig. 9 shows the schematic representation of the laser cladding process. There is no doubt that this process involves strongly coupled

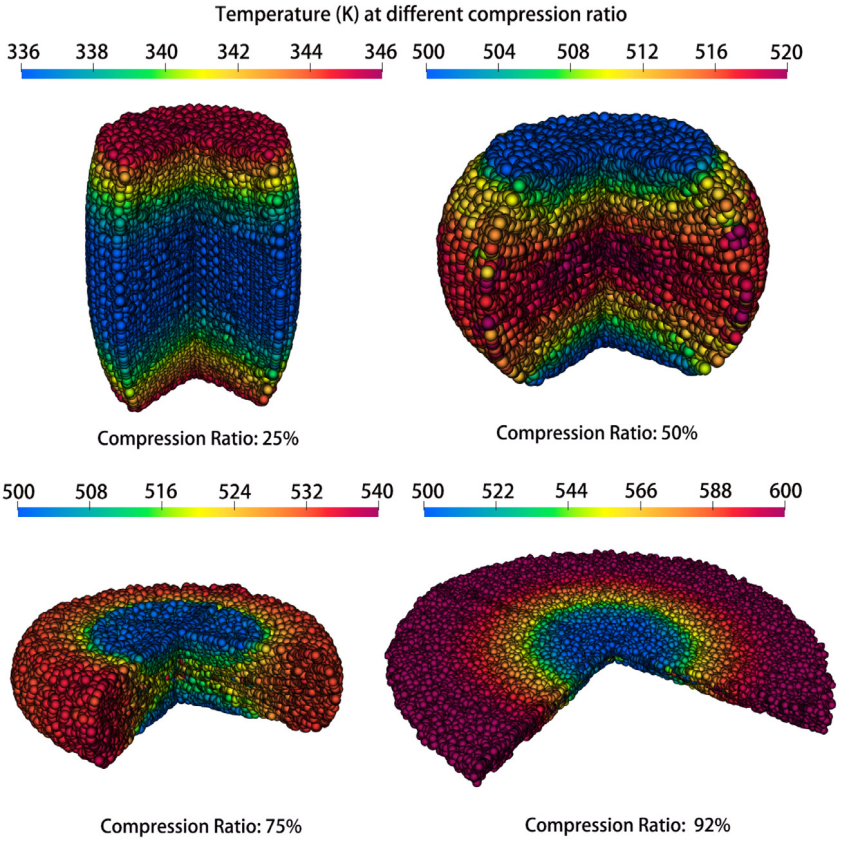

Fig. 7. HOTM simulation results of the hot compression case: evolution of the temperature field and deformed configuration at compression ratio 25%, 50%, 75% and 95%, with a maximum temperature increase of 310 K.

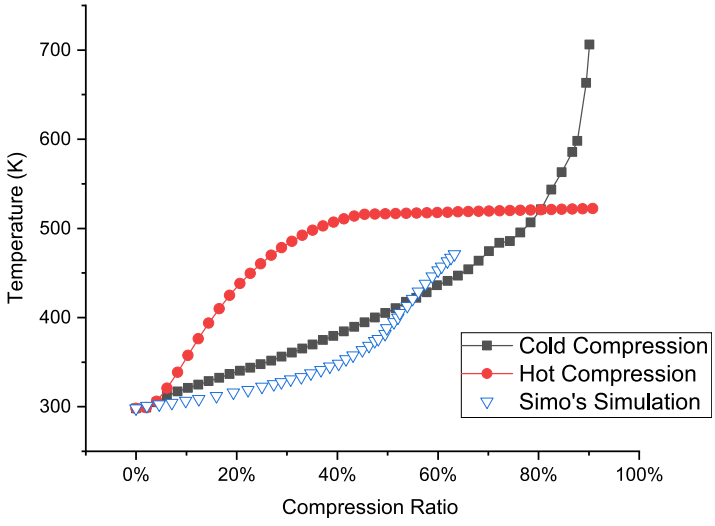

Fig. 8. The evolution of temperature at the center of the billet during compression.

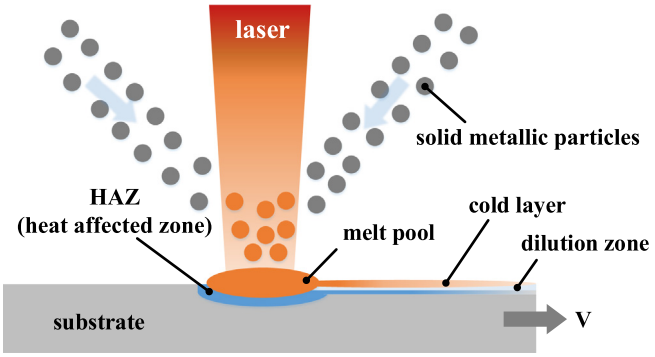

Fig. 9. (a) Schematic representation of the laser cladding process.

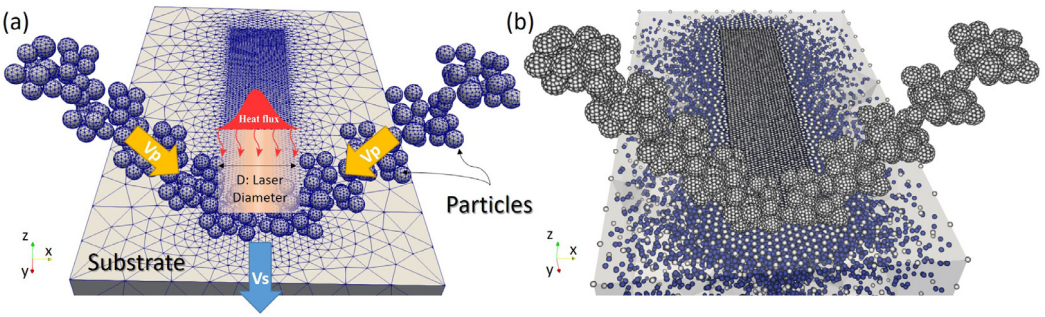

Fig. 10. The initial configuration of the powder particles and the substrate in the HOTM simulation of laser cladding process: (a) triangulation representation of the geometry; (b) meshfree representation with material points and nodes.

multi-physics phenomena, including heat conduction, convection and radiation heat transfer, dynamic contact, free-surface and surface tension, phase transition and fluid–structure interaction [5,6]. The simulation of such problems by Eulerian methods and grid-based Lagrangian methods is extremely challenging. In our last example, we demonstrate the robustness and efficiency of the HOTM method in simulating the strongly coupled thermomechanical problem during the laser cladding process.

Fig. 10 depicts the initial configuration of the powder particles and the substrate in a triangulation and meshfree representation, respectively. For simplicity, two beams of powder particles are simulated instead of tapered full-ring of powder. There are 200 particles explicitly modeled in our simulations, each of which is discretized by more than 500 material points placed at the barycenters of the initial tetrahedral elements and 720 degrees of freedom. The radii of the particles are ranged from 10 μm to 30 μm with a Gaussian distribution centered at 20 μm obtained from experimental statistics. The substrate with the dimension of 1600 μm × 1000 μm × 900 μm is modeled by 67,200 material points and 61,836 degrees of freedom adaptively. The spherical particles strike the substrate obliquely at an initial speed of V_p, which travels at a constant speed V_s in the y-direction. The laser beam is modeled as a moving heat flux subjected to the surface of particles and the substrate. Various models to describe the energy distribution of heat source exist in the literature. Detailed reviews can be found in [7]. In our simulations, the Gaussian form of

$$\bar{h} = 2\frac{AP}{\pi r^2}\exp\left(-2\frac{(x-x_c(t))^2+(y-y_c(t))^2}{r^2}\right), \quad \text{if } (x-x_c(t))^2+(y-y_c(t))^2 < r^2 \tag{93}$$

is employed to describe the heat flux where A is the absorptivity of the material, P is the laser power, x_c and y_c are the coordinates of the laser center, and r is the radius of the laser beam. The heat flux of the laser power is applied to nodes on the surface of particles and the substrate dynamically. We introduce a simple algorithm to find the set of heat flux nodes. In specific, we first decompose the space into a number of equally spaced columns parallel to

the direction of the laser ray, $\hat{\boldsymbol{N}}_L$, based on a user-defined spacing factor δ. A set of surface nodes, $\mathcal{S}$, is formed by selecting the surface node with the maximum component in the direction of $\hat{\boldsymbol{N}}_L$ within each column. Thus, the set of heat flux nodes is defined as

$$\mathcal{M} = \{\boldsymbol{x}_a \mid \boldsymbol{x}_a \in \mathcal{S}, \text{ and } \| \boldsymbol{x}_a - \boldsymbol{x}_c \| \leq r, \text{ and } \hat{\boldsymbol{N}}(\boldsymbol{x}_a) \cdot \hat{\boldsymbol{N}}_L < 0\}, \tag{94}$$

where $\hat{\boldsymbol{N}}(\boldsymbol{x}_a)$ is the current normal direction of node $\boldsymbol{x}_a$. Reflection of the laser ray from the surfaces is not taken into account in our definition, since the particles travel very fast in air and only a sparse distribution of powder is considered in this example. A more comprehensive solution to find the heat flux nodes and determine the local laser power can be obtained by using the ray tracing algorithm [73]. It can be seen from Eq. (93) that only nodes in the radius of r are irradiated by the laser beam, and other parts of the computational domain are heated up through heat conduction. In addition, convective heat conduction is applied to all the free surface nodes following the simple form

$$\bar{h} = k_c(T - T_{\text{env}}), \tag{95}$$

where k_c and T_{env} are the convective heat conduction coefficient and environment temperature, respectively. Within the Lagrangian framework, nodes on the free surfaces in the reference configuration remain as surface nodes unless they are in contact with neighboring surface nodes. We further assume there is no new surface nodes generated for receiving the heat flux during the laser cladding process since we do not allow fracture or separation in this study. Considering a nodal integration scheme for the surface integrals, the external thermal driving forces due to the heat flux are obtained as

$$Q^{ext}_{a,n+1} = \Delta t \frac{\bar{h}_{a,n+1}}{T_{a,n+1}} A_{a,n}. \tag{96}$$

Meanwhile, the effect of surface tension is taken into account as a traction boundary condition, which follows the conventional form [74]

$$\bar{\mathbf{T}}(T) = -\sigma(T)\kappa\hat{\boldsymbol{N}}, \tag{97}$$

where $\sigma(T)$ is the temperature-dependent surface tension coefficient, κ and $\hat{\boldsymbol{N}}$ are the surface curvature and normal direction, respectively. A nodal integration on the free surface gives the external mechanical nodal forces due to the surface tension as

$$\boldsymbol{f}^{ext}_{a,n+1} = \bar{\mathbf{T}}_{a,n+1} A_{a,n}, \tag{98}$$

where $\bar{\mathbf{T}}_{a,n+1}$ is the nodal traction, and the weight $A_{a,n}$ can be interpreted as the surface area of Γ_t tributary to node $\boldsymbol{x}_a$. The surface area and normal direction of a free surface node $\boldsymbol{x}_a$ in the current configuration is determined by the Piola transformation incrementally,

$$A_{a,n+1}\hat{\boldsymbol{N}}_{a,n+1} = J_{n\to n+1}\boldsymbol{F}^{-1}_{n\to n+1} A_{a,n}\hat{\boldsymbol{N}}_{a,n}, \tag{99}$$

where $J_{n\to n+1}$ and $\boldsymbol{F}_{n\to n+1}$ are the incremental Jacobian and deformation gradient from t_n to t_{n+1}, respectively. The current curvature $\kappa_{a,n+1}$ of a surface node $\boldsymbol{x}_a$ is determined by extending the approximation scheme proposed in [75]. In our calculations, a search algorithm is employed to find the neighboring surface nodes of $\boldsymbol{x}_a$, i.e., $\mathcal{S}_{n+1} = \{\boldsymbol{x}_{b,n+1} \in \Gamma, \text{ s.t. } |\boldsymbol{x}_{b,n+1} - \boldsymbol{x}_{a,n+1}| \leq d\}$, where Γ is the free surface of the melted material. Thus, the normal curvature at $\boldsymbol{x}_a$ with respect to individual neighboring nodes in $\mathcal{S}_{n+1}$ can be calculated as

$$\kappa_{i,n+1} = -\frac{(\boldsymbol{x}_{i,n+1} - \boldsymbol{x}_{a,n+1}) \cdot (\hat{\boldsymbol{N}}_{i,n+1} - \hat{\boldsymbol{N}}_{a,n+1})}{\| \boldsymbol{x}_{i,n+1} - \boldsymbol{x}_{a,n+1} \|^2} \quad \text{where } \boldsymbol{x}_i \in \mathcal{S}_{n+1}. \tag{100}$$

The principal curvatures, κ_1 and κ_2 at node $\boldsymbol{x}_a$, are then approximated by using the least square method from the set of individual curvatures $\{\kappa_{i,n+1}\}$ [75]. Finally, the current curvature is obtained as $\kappa_{a,n+1} = \kappa_1 + \kappa_2$. This algorithm applied in a meshfree manner is validated using the examples proposed in [75]. The validation results show that the accuracy of the calculated curvature improves as the number of neighboring surface nodes are involved in the approximation.

The material of the particles and the substrate is Stainless Steel S390 and modeled by the constitutive equations (30) and (45). In specific, we ignore the plastic deformation as the particles in solid phase and consider weak

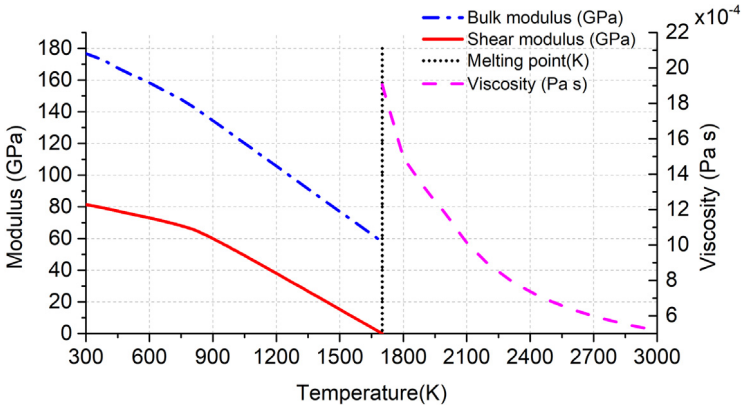

Fig. 11. Materials mechanical properties versus temperature.

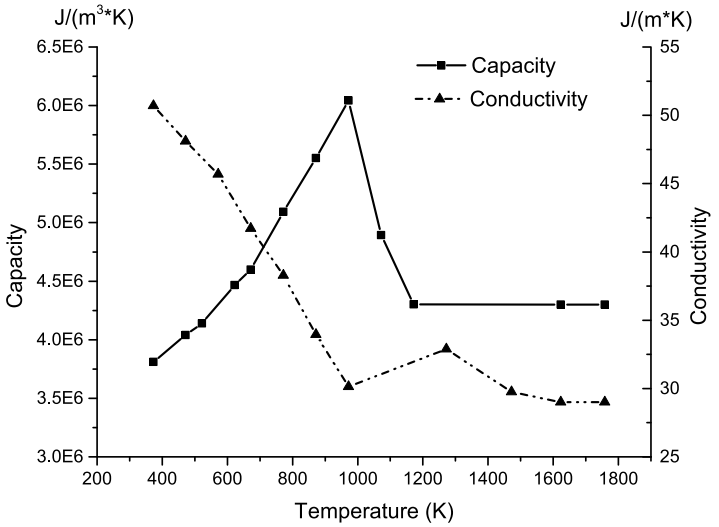

Fig. 12. Materials thermal properties versus temperature.

Table 5
Material parameters of stainless steel S390 used in the test cases.

Density ρ_0 (kg/m^3)	Melting temperature T_m (K)	Boiling temperature T_b (K)	Latent heat melting L_m (kJ/kg)	Latent heat vaporization L_b (kJ/kg)	Convective heat conduction coefficient k_c (W/K m^2)	Surface tension coefficient σ (N/m)
7800	1700	3000	247	6090	50	1.887

compressibility in the fluid phase, which indicates a thermo-visco-elastic response of the material. The bulk modulus $K(T)$, shear modulus $\mu(T)$, viscosity coefficient $\eta(T)$, heat conductivity coefficient $\kappa(T)$ and specific heat capacity $C(T)$ are all temperature dependent functions and calibrated by fitting to experimental data, as shown in Figs. 11 and 12. The rest of the important material properties are listed in Table 5.

Key processing parameters, such as laser power, laser radius, particle and substrate travel velocity play an important role in the melt pool thermodynamics. They further determine the performance of the cladding. In our tests, we fix the laser power and radius but vary the feeding angle of powder and the travel speed of the substrate. Four test cases were performed based on the HOTM method to investigate the influence of the process parameters

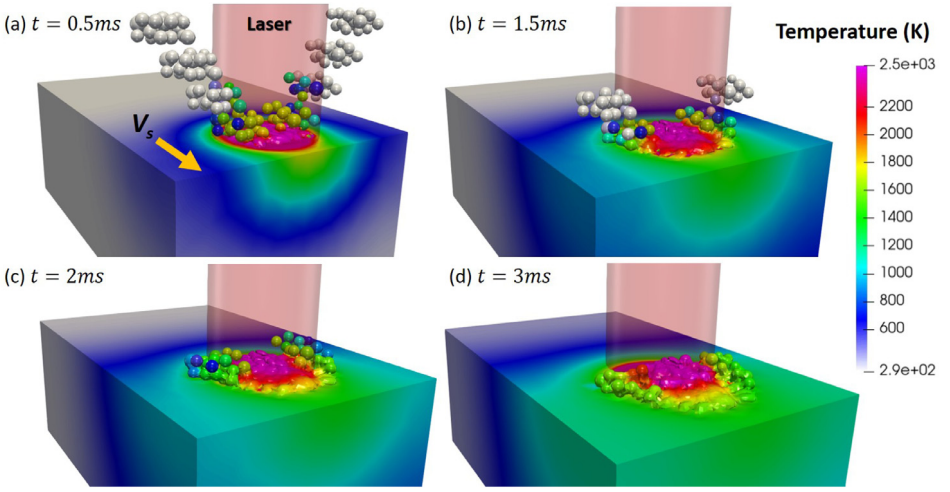

Fig. 13. Snapshots of the predicted deformed configuration and temperature distribution in the powder particles and the substrate at $V_s = 0.1$ m/s.

Table 6
Processing parameters in the simulation of laser cladding technology.

Laser power P (W)	Laser radius r (μm)	Laser center (x_c, y_c) (μm)	Powder feeding speed V_p (m/s)	Absorptivity in solid phase A	Absorptivity in liquid phase A
1500	200	(−200, 0)	0.3	0.1	0.2

on the dimensions of the meltpool and cladding, including thickness, length and width. The processing parameters are summarized in Table 6. The travel speed of the substrate, V_s, is chosen from the range of 0.1 m/s to 0.8 m/s.

Fig. 13 shows the time evolution of the deformed configuration and temperature distribution in the particles and the substrate during the laser cladding process at $V_s = 0.1$ m/s. With the aid of the direct numerical simulation based on the HOTM method, a detailed description of the temperature, phase and shape evolution of the particles and the substrate is obtained. As the particles travel in air and enter the range of the laser, their temperature rises up. Since the particles in air are discrete without contacting to each other, the laser power is all converted to their internal energy, which heats up the particles quickly beyond the melting temperature. When the local temperature at a material point reaches the melting temperature, the material point transits to fluid phase. If the laser power is intensive, the entire particle may melt after the heat transfers from the heat flux boundary to the interior, otherwise it remains as a solid or partially melted. While the heat contained in the particles transfers to the environment through convection, the longer the particles are radiated by the laser beam the higher is their temperature as indicated by the temperature distribution in the powder beam. Since the powder beam is fed to the substrate at an angle, some of the particles outside of the range of the laser beam remain as solid until they are in contact with the hot particles and the substrate. However, due to low body forces, before the particles strike the substrate, they remain the spherical shape even though turning into the liquid phase. Meanwhile, the laser beam penetrates the powder region and continuously input energy to the substrate. As demonstrated in Fig. 14, a shallow meltpool forms on the surface of the substrate. When the melted particles impact the surface of the substrate, they spread out and merge into the meltpool to create a coating layer. Subjected to the impact forces, the substrate material in the meltpool is compressed. Due to the slow travel speed of the substrate, the powder material piles up and pushes the molten substrate material to form a bump on the surface. As a consequence, the roughness of the coated surface increases. The formation mechanism of the cladding and thermomechanical responses of the material are made clear in the cross-section snapshots of the domain in Fig. 15. it is worth mentioning that the mixing of the melted particles and the substrate as well as the interaction between the melt pool and unmelted or partially melted particles are well captured in the HOTM simulations. On the other hand, the heat transfer among particles and between particles and the substrate caused by the dynamic contact is a natural outcome of the thermomechanical coupling meshfree method, which challenges Eulerian methods greatly.

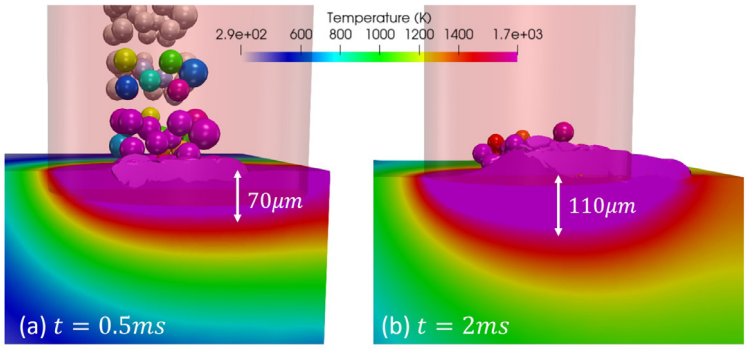

Fig. 14. Cross-section of the predicted meltpool on the substrate as it travels at $V_s = 0.1$ m/s.

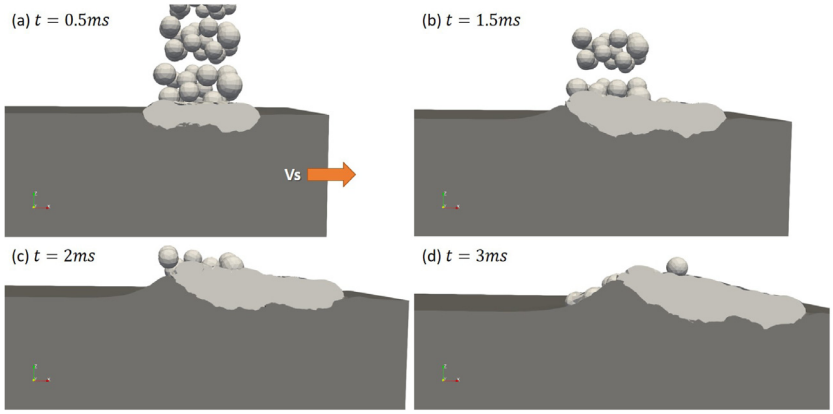

Fig. 15. Snapshots of the cladding process $V_s = 0.1$ m/s predicted by the HOTM method where the substrate is in dark gray and the powder material in light gray.

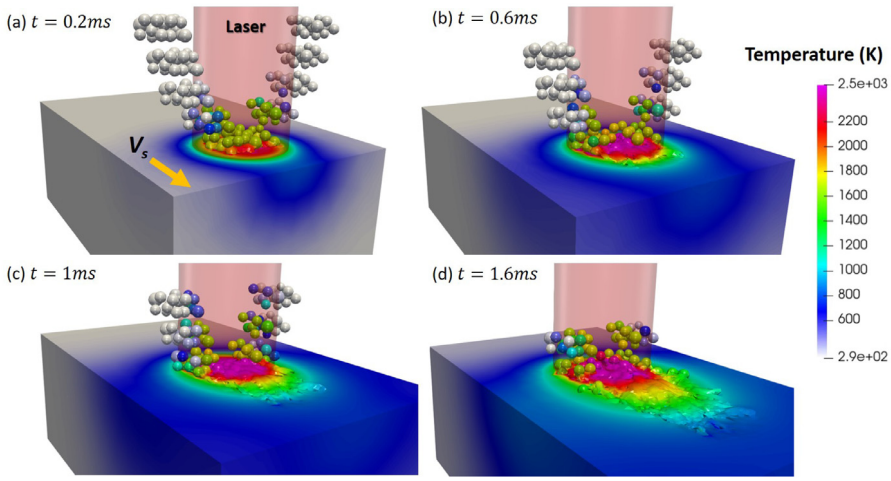

Fig. 16. Snapshots of the predicted deformed configuration and temperature distribution in the powder particles and the substrate at $V_s = 0.4$ m/s.

As we increase the travel speed of the substrate to $V_s = 0.4$ m/s in Fig. 16, there is less energy absorbed by the substrate from the laser beam, such that the temperature in the substrate is lower than the one in the test of

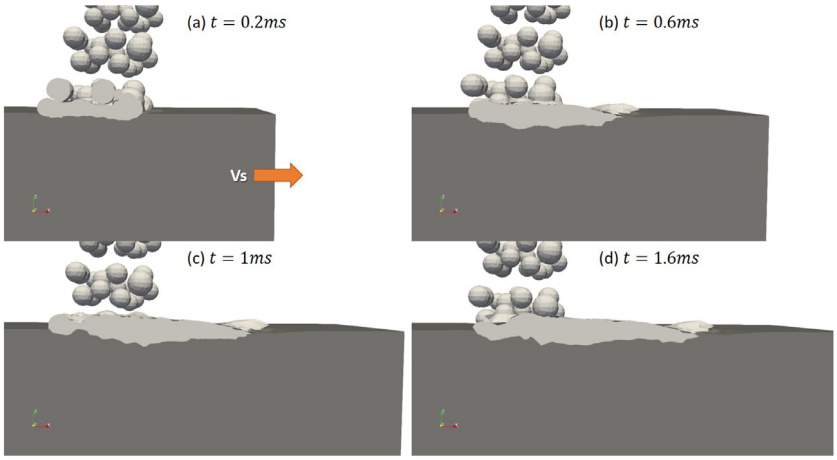

Fig. 17. Snapshots of the cladding process at $V_s = 0.4$ m/s predicted by the HOTM method where the substrate is in dark gray and the powder material in light grey.

$V_s = 0.1$ m/s. The increased relative speed also gives rise to extensive deformation of the liquid particles which can flow on the substrate more easily. It can be observed in the cross section of the meltpool in Fig. 17 that the coating layer on the substrate becomes thinner and more flat comparing to the one with a slower travel speed. Overall, this process involves large deformation, transient heat transfer, phase transition, free surface boundary conditions, dynamic contact and fluid–structure interaction, which further relies on the processing parameters. Note that only the first couple of milliseconds of the impact process is studied in these simulations. The inertia effects, deformation of the liquid particles as well as the fusion of droplets and the melt pool are the dominant responses of the domain. Besides, the variation of temperature on the surface of the melt pool near the contact region is not significant within this short period of impact, as shown in Figs. 13 and 16. Thus, the tangential surface gradient of the surface tension is neglected in Eq. (97). As a result, the Marangoni effect induced by the gradient of surface tension is not noticeable in our simulations. The influence of the substrate travel speed on the cladding thickness calculated in the HOTM simulations is plot in Fig. 18. The correlation between the axial feed velocity and the layer thickness predicted by the HOTM simulations is consistent with the experimental observations in [76]. The direct numerical simulation of the laser cladding process at the powder scale exhibits the full range of the HOTM method in dealing with unconstrained material flows under extreme thermomechanical coupling conditions.

4. Conclusion

We have developed a monolithic Lagrangian meshfree method, the Hot Optimal Transportation Meshfree (HOTM) method, for the high fidelity prediction of the dynamic responses of materials under extreme thermo-mechanical coupling conditions, possibly involving extremely large deformation, phase transition and multiphase mixing in three-dimensions. The HOTM method combines the Optimal Transportation Meshfree (OTM) method and the variational thermomechanical constitutive updates. By introducing the optimal transportation theory for the time discretization and material point sampling as the spatial discretization scheme, we obtained the full discrete mechanical and thermal balance equations in a meshfree manner from the stationarity condition of the variational formulation of a dynamic thermomechanical system. The operator splitting algorithm is employed to solve the system of balance equations in a staggered fashion. In specific, at each time increment, the mechanical balance equations are solved explicitly, while a fully implicit solution using the Newton–Raphson iterations is employed for the thermal balance equations. Consequently, the deformation, temperature, and internal state variables are obtained simultaneously for a strongly coupled thermomechanical system with general dissipation mechanisms, arbitrary three-dimensional geometry, and boundary conditions. Moreover, in response to the extreme thermomechanical conditions, materials usually experience finite deformations and high temperature variations, which often results in highly nonlinear inelastic behavior and phase change, such as melting, vaporization, and solidification. Based on the local thermodynamic models, we constructed a specific form for the thermoviscoplastic behavior of materials,

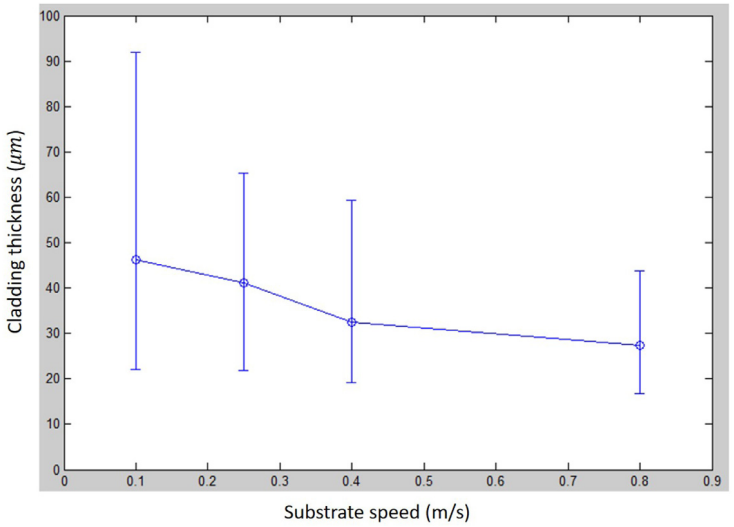

Fig. 18. The cladding thickness as a function of the travel speed of the substrate calculated in the HOTM simulations.

such as metals, covering the solid, liquid and gas phases, and allowing to study the partition of plastic work in stored and dissipated energy systematically. The convergence property of the HOTM method is studied in a three-dimensional transient heat transfer problem. The accuracy of the HOTM method is depicted in the test of a cylinder under compression and thermal boundary conditions by a direct comparison of the predicted temperature change to the simulation results presented in Simo et al. [8]. Finally, the robustness and scope of the HOTM method in the modeling of materials under extreme thermomechanical conditions are demonstrated in the application of the laser cladding technology of metals.

Nevertheless, we have introduced some thermodynamic inconsistency in the constitutive relation for the material during phase transition. Notably, the inclusion of the latent heat using the apparent heat capacity method violates the relationship between heat capacity and the Helmholtz free energy density. On the other hand, material properties exhibit nonlinear dependence on the temperature as observed in experimental measurements. The effects of the variation of material properties due to the temperature change during phase transition are not explicitly accounted for in the thermal balance equations. Also, the introduction of a phase transition strain in the kinematics may enable a better description of the stress change for the material in the mushy zone. Finally, in our last example of the HOTM simulation of laser cladding processes, the calculation of surface properties, such as the curvature and surface traction, including surface tension and recoil pressure, in a meshfree framework needs to be further studied. As has been commonly recognized, the Marangoni effect induced by the gradient of surface tension is one of the most critical responses of the melt pool. High fidelity prediction of the Marangoni convection necessitates an accurate calculation of the local temperature-dependent surface tension forces as well as their tangential surface gradient. It may be an excellent alternative to track the interface and compute the surface properties using a color function [44,74].

Acknowledgment

The authors would like to gratefully acknowledge the financial support of the National Science Foundation, USA Early Career Award NSF/CMMI 1652839.

References

[1] L.-E. Lindgren, Numerical modelling of welding, Comput. Methods Appl. Mech. Engrg. 195 (48–49) (2006) 6710–6736.
[2] V.M. Joy Varghese, M.R. Suresh, D. Siva Kumar, Recent developments in modeling of heat transfer during tig welding—a review, Int. J. Adv. Manuf. Technol. 64 (5–8) (2013) 749–754.
[3] AE Huespe, ALBERTO Cardona, VICTOR Fachinotti, Thermomechanical model of a continuous casting process, Comput. Methods Appl. Mech. Engrg. 182 (3–4) (2000) 439–455.

[4] Chunsheng Li, Brian G. Thomas, Thermomechanical finite-element model of shell behavior in continuous casting of steel, Metall. Mater. Trans. B 35 (6) (2004) 1151–1172.
[5] Kaufui V. Wong, Aldo Hernandez, A review of additive manufacturing, ISRN Mech. Eng. 2012 (2012).
[6] William E. Frazier, Metal additive manufacturing: a review, J. Mater. Eng. Perform. 23 (6) (2014) 1917–1928.
[7] Babis Schoinochoritis, Dimitrios Chantzis, Konstantinos Salonitis, Simulation of metallic powder bed additive manufacturing processes with the finite element method: A critical review, Proc. Inst. Mech. Eng. B 231 (1) (2017) 96–117.
[8] J.C. Simo, Ch. Miehe, Associative coupled thermoplasticity at finite strains: Formulation, numerical analysis and implementation, Comput. Methods Appl. Mech. Engrg. 98 (1) (1992) 41–104.
[9] G. Zavarise, P. Wriggers, E. Stein, B.A. Schrefler, Real contact mechanisms and finite element formulation—a coupled thermomechanical approach, Internat. J. Numer. Methods Engrg. 35 (4) (1992) 767–785.
[10] L.M. Galantucci, L. Tricarico, Thermo-mechanical simulation of a rolling process with an fem approach, J. Mater Process. Technol. 92 (1999) 494–501.
[11] C.M. Chen, R. Kovacevic, Finite element modeling of friction stir welding—thermal and thermomechanical analysis, Int. J. Mach. Tools Manuf. 43 (13) (2003) 1319–1326.
[12] B. Peultier, T. Ben Zineb, E. Patoor, Macroscopic constitutive law of shape memory alloy thermomechanical behaviour. application to structure computation by fem, Mech. Mater. 38 (5–6) (2006) 510–524.
[13] Scott F. Miller, Albert J. Shih, Thermo-mechanical finite element modeling of the friction drilling process, J. Manuf. Sci. Eng. 129 (3) (2007) 531–538.
[14] Jean Donea, P. Fasoli-Stella, S. Giuliani, Lagrangian and Eulerian Finite Element Techniques for Transient Fluid-Structure Interaction Problems, IASMiRT, 1977.
[15] Jean Donea, S. Giuliani, Jean-Pierre Halleux, An arbitrary lagrangian-eulerian finite element method for transient dynamic fluid-structure interactions, Comput. Methods Appl. Mech. Engrg. 33 (1–3) (1982) 689–723.
[16] Lars Olovsson, Larsgunnar Nilsson, Kjell Simonsson, An ale formulation for the solution of two-dimensional metal cutting problems, Comput. Struct. 72 (4–5) (1999) 497–507.
[17] M.S. Gadala, Recent trends in ale formulation and its applications in solid mechanics, Comput. Methods Appl. Mech. Engrg. 193 (39–41) (2004) 4247–4275.
[18] G.R. Liu, M.B. Liu, Shaofan Li, Smoothed particle hydrodynamics—a meshfree method, Comput. Mech. 33 (6) (2004) 491.
[19] Jérôme Limido, Christine Espinosa, Michel Salaün, Jean-Luc Lacome, Sph method applied to high speed cutting modelling, Int. J. Mech. Sci. 49 (7) (2007) 898–908.
[20] R. Das, P.W. Cleary, Novel application of the mesh-free sph method for modelling thermo-mechanical responses in arc welding, Int. J. Mech. Mater. Des. 11 (3) (2015) 337–355.
[21] E. Onate, J. Rojek, Combination of discrete element and finite element methods for dynamic analysis of geomechanics problems, Comput. Methods Appl. Mech. Engrg. 193 (27–29) (2004) 3087–3128.
[22] Peter Eberhard, Timo Gaugele, Simulation of cutting processes using mesh-free lagrangian particle methods, Comput. Mech. 51 (3) (2013) 261–278.
[23] Eckart Uhlmann, Robert Gerstenberger, Jörg Kuhnert, Cutting simulation with the meshfree finite pointset method, Procedia CIRP 8 (2013) 391–396.
[24] Edgar O. Reséndiz-Flores, Félix R. Saucedo-Zendejo, Two-dimensional numerical simulation of heat transfer with moving heat source in welding using the finite pointset method, Int. J. Heat Mass Transfer 90 (2015) 239–245.
[25] Y.Y. Lu, T. Belytschko, Lu Gu, A new implementation of the element free galerkin method, Comput. Methods Appl. Mech. Engrg. 113 (3–4) (1994) 397–414.
[26] H.S. Wang, A meshfree variational multiscale methods for thermo-mechanical material failure, Theor. Appl. Fract. Mech. 75 (2015) 1–7.
[27] Wing Kam Liu, Sukky Jun, Shaofan Li, Jonathan Adee, Ted Belytschko, Reproducing kernel particle methods for structural dynamics, Internat. J. Numer. Methods Engrg. 38 (10) (1995) 1655–1679.
[28] J.K. Chen, J.E. Beraun, T.C. Carney, A corrective smoothed particle method for boundary value problems in heat conduction, Internat. J. Numer. Methods Engrg. 46 (2) (1999) 231–252.
[29] Chen Li, Ma He-Ping, Cheng Yu-Min, Combining the complex variable reproducing kernel particle method and the finite element method for solving transient heat conduction problems, Chin. Phys. B 22 (5) (2013) 050202.
[30] Elias Cueto, Francisco Chinesta, Meshless methods for the simulation of material forming, Int. J. Mater. Form. 8 (1) (2015) 25–43.
[31] Seyed Mahmoud Hosseini, Jan Sladek, Vladimir Sladek, Meshless local petrov–galerkin method for coupled thermoelasticity analysis of a functionally graded thick hollow cylinder, Eng. Anal. Bound. Elem. 35 (6) (2011) 827–835.
[32] Baodong Dai, Baojing Zheng, Qingxiang Liang, Linghui Wang, Numerical solution of transient heat conduction problems using improved meshless local petrov–galerkin method, Appl. Math. Comput. 219 (19) (2013) 10044–10052.
[33] J.M. Rodriguez, J.M. Carbonell, J.C. Cante, J. Oliver, The particle finite element method (pfem) in thermo-mechanical problems, Internat. J. Numer. Methods Engrg. 107 (9) (2016) 733–785.
[34] Deborah Sulsky, Zhen Chen, Howard L. Schreyer, A particle method for history-dependent materials, Comput. Methods Appl. Mech. Engrg. 118 (1–2) (1994) 179–196.
[35] E. Love, Deborah L. Sulsky, An unconditionally stable, energy–momentum consistent implementation of the material-point method, Comput. Methods Appl. Mech. Engrg. 195 (33–36) (2006) 3903–3925.
[36] Duan Z. Zhang, Qisu Zou, W. Brian VanderHeyden, Xia Ma, Material point method applied to multiphase flows, J. Comput. Phys. 227 (6) (2008) 3159–3173.

[37] Jiun-Shyan Chen, Michael Hillman, Sheng-Wei Chi, Meshfree methods: progress made after 20 years, J. Eng. Mech. 143 (4) (2017) 04017001.
[38] B. Li, F. Habbal, M. Ortiz, Optimal transportation meshfree approximation schemes for fluid and plastic flows, Internat. J. Numer. Methods Engrg. 83 (12) (2010) 1541–1579.
[39] B. Li, A. Kidane, G. Ravichandran, M. Ortiz, Verification and validation of the optimal transportation meshfree (otm) simulation of terminal ballistics, Int. J. Impact Eng. 42 (2012) 25–36.
[40] A Kidane, A Lashgari, B Li, M McKerns, M Ortiz, H Owhadi, G Ravichandran, M Stalzer, TJ Sullivan, Rigorous model-based uncertainty quantification with application to terminal ballistics, part i: Systems with controllable inputs and small scatter, J. Mech. Phys. Solids 60 (5) (2012) 983–1001.
[41] M Adams, A Lashgari, B Li, M McKerns, J Mihaly, M Ortiz, H Owhadi, AJ Rosakis, M Stalzer, TJ Sullivan, Rigorous model-based uncertainty quantification with application to terminal ballistics-part ii. Systems with uncontrollable inputs and large scatter, J. Mech. Phys. Solids 60 (5) (2012) 1002–1019.
[42] P-HT Kamga, B Li, M McKerns, LH Nguyen, M Ortiz, H Owhadi, TJ Sullivan, Optimal uncertainty quantification with model uncertainty and legacy data, J. Mech. Phys. Solids 72 (2014) 1–19.
[43] Rishi Ganeriwala, Tarek I. Zohdi, A coupled discrete element-finite difference model of selective laser sintering, Granul. Matter 18 (2) (2016) 21.
[44] M.A. Russell, A. Souto-Iglesias, and TI3845621 Zohdi, Numerical simulation of laser fusion additive manufacturing processes using the sph method, Comput. Methods Appl. Mech. Engrg. 341 (2018) 163–187.
[45] Jan-Philipp Fürstenau, Henning Wessels, Christian Weißenfels, Peter Wriggers, Generating virtual process maps of slm using powder-scale sph simulations, Comput. Part. Mech. (2019) 1–23.
[46] H. Wessels, C. Weißenfels, P. Wriggers, Metal particle fusion analysis for additive manufacturing using the stabilized optimal transportation meshfree method, Comput. Methods Appl. Mech. Engrg. 339 (2018) 91–114.
[47] H. Wessels, T. Bode, C. Weißenfels, P. Wriggers, T.I. Zohdi, Investigation of heat source modeling for selective laser melting, Comput. Mech. 63 (5) (2019) 949–970.
[48] Jean-David Benamou, Yann Brenier, A computational fluid mechanics solution to the monge-kantorovich mass transfer problem, Numer. Math. 84 (3) (2000) 375–393.
[49] Marino Arroyo, Michael Ortiz, Local maximum-entropy approximation schemes: a seamless bridge between finite elements and meshfree methods, Internat. J. Numer. Methods Engrg. 65 (13) (2006) 2167–2202.
[50] Mathieu Foca, On a Local Maximum Entropy Interpolation Approach for Simulation of Coupled Thermo-Mechanical Problems. Application to the Rotary Frictional Welding Process, (PhD thesis), Ecole Centrale de Nantes (ECN), 2015.
[51] C. Weißenfels, P. Wriggers, Stabilization algorithm for the optimal transportation meshfree approximation scheme, Comput. Methods Appl. Mech. Engrg. 329 (2018) 421–443.
[52] Jiang Fan, Huming Liao, Renjie Ke, Erdem Kucukal, Umut A Gurkan, Xiuli Shen, Jian Lu, Bo Li, A monolithic lagrangian meshfree scheme for fluid–structure interaction problems within the otm framework, Comput. Methods Appl. Mech. Engrg. 337 (2018) 198–219.
[53] Qiang Yang, Laurent Stainier, Michael Ortiz, A variational formulation of the coupled thermo-mechanical boundary-value problem for general dissipative solids, J. Mech. Phys. Solids 54 (2) (2006) 401–424.
[54] Laurent Stainier, Michael Ortiz, Study and validation of a variational theory of thermo-mechanical coupling in finite visco-plasticity, Int. J. Solids Struct. 47 (5) (2010) 705–715.
[55] Laurent Stainier, Consistent incremental approximation of dissipation pseudo-potentials in the variational formulation of thermo-mechanical constitutive updates, Mech. Res. Commun. 38 (4) (2011) 315–319.
[56] Laurent Stainier, A variational approach to modeling coupled thermo-mechanical nonlinear dissipative behaviors, in: Advances in Applied Mechanics, Vol. 46, Elsevier, 2013, pp. 69–126.
[57] Zongyue Fan, Bo Li, Meshfree simulations for additive manufacturing process of metals, Integr. Mater. Manuf. Innov. 8 (2) (2019) 144–153.
[58] Bernard Halphen, Quoc Son Nguyen, Sur les matériaux standard généralisés, J. Méc. 14 (1975) 39–63.
[59] H. Ziegler, An Introduction to Thermomechanics, North-Holland, 1977.
[60] Erastus H. Lee, Elastic-plastic deformation at finite strains, J. Appl. Mech. 36 (1) (1969) 1–6.
[61] Heinrich Hencky, Uber die form des elastizitatsgesetzes bei ideal elastischen stoffen, Z. Tech. Phys. 9 (1928) 215–220.
[62] Vlado A. Lubarda, Elastoplasticity Theory, CRC press, 2001.
[63] S.P. Lyon, J.D. Johnson, The Los Alamos National Laboratory EOS Database Report No, Technical report, LA-UR-92-3407, 1992.
[64] Comini Bonacina, G. Comini, A. Fasano, and M 1973 Primicerio, Numerical solution of phase-change problems, Int. J. Heat Mass Transfer 16 (10) (1973) 1825–1832.
[65] Maurice Antony Biot, et al., Linear thermodynamics and the mechanics of solids, in: Proceedings of the Third US National Congress of Applied Mechanics, American Society of Mechanical Engineers, Citeseer, 1958.
[66] Jason Har, Kumar Tamma, Advances in Computational Dynamics of Particles, Materials and Structures, John Wiley & Sons, 2012.
[67] Robert J. McCann, A convexity principle for interacting gases, Adv. Math. 128 (1) (1997) 153–179.
[68] Jiang Fan, Huming Liao, Hao Wang, Junheng Hu, Zhiying Chen, Jian Lu, Bo Li, Local maximum-entropy based surrogate model and its application to structural reliability analysis, Struct. Multidiscip. Optim. 57 (1) (2018) 373–392.
[69] Adam Amar, Nathan Calvert, Benjamin Kirk, Development and verification of the charring ablating thermal protection implicit system solver, in: 49th AIAA Aerospace Sciences Meeting Including the New Horizons Forum and Aerospace Exposition, 2011, p. 144.
[70] Adrian Bejan, Allan D. Kraus, Heat Transfer Handbook, Vol. 1, John Wiley & Sons, 2003.
[71] Vedat S. Arpaci, Conduction Heat Transfer, Addison-Wesley, 1966.

[72] J. Mazumder, 1 - laser-aided direct metal deposition of metals and alloys, in: Milan Brandt (Ed.), Laser Additive Manufacturing, in: Woodhead Publishing Series in Electronic and Optical Materials, Woodhead Publishing, 2017, pp. 21–53.
[73] Wim Devesse, Dieter De Baere, Patrick Guillaume, Modeling of laser beam and powder flow interaction in laser cladding using ray-tracing, J. Laser Appl. 27 (S2) (2015) S29208.
[74] Jeremiah U. Brackbill, Douglas B. Kothe, Charles Zemach, A continuum method for modeling surface tension, J. Comput. Phys. 100 (2) (1992) 335–354.
[75] Chen-shi Dong, Guo-zhao Wang, Curvatures estimation on triangular mesh, J. Zhejiang Univ.-Sci. A 6 (1) (2005) 128–136.
[76] T. Schopphoven, A. Gasser, K. Wissenbach, R. Poprawe, Investigations on ultra-high-speed laser material deposition as alternative for hard chrome plating and thermal spraying, J. Laser Appl. 28 (2) (2016) 022501.